nature communications

Article

https://doi.org/10.1038/s41467-025-56873-z

Co-translational protein aggregation and ribosome stalling as a broad-spectrum antibacterial mechanism

Received: 11 March 2024

Accepted: 30 January 2025

Published online: 12 February 2025

Check for updates

Laleh Khodaparast[1,2,8], Ladan Khodaparast[1,2,8], Ramon Duran-Romaña[1,2], Guiqin Wu[1,2], Bert Houben[1,2], Wouter Duverger[1,2], Matthias De Vleeschouwer[1,2], Katerina Konstantoulea[1,2], Fleur Nysen[1,2], Thomas Schalck[3,4], Daniel J. Curwen[5], Lisandra L. Martin[5], Sebastien Carpentier[6], Bernard Scorneaux[7], Jan Michiels[3,4], Joost Schymkowitz[1,2] ✉ & Frederic Rousseau[1,2] ✉

Drug-resistant bacteria pose an urgent global health threat, necessitating the development of antibacterial compounds with novel modes of action. Protein biosynthesis accounts for up to half of the energy expenditure of bacterial cells, and consequently inhibiting the efficiency or fidelity of the bacterial ribosome is a major target of existing antibiotics. Here, we describe an alternative mode of action that affects the same process: allowing translation to proceed but causing co-translational aggregation of the nascent peptidic chain. We show that treatment with an aggregation-prone peptide induces formation of polar inclusion bodies and activates the SsrA ribosome rescue pathway in bacteria. The inclusion bodies contain ribosomal proteins and ribosome hibernation factors, as well as mRNAs and cognate nascent chains of many proteins in amyloid-like structures, with a bias for membrane proteins with a fold rich in long-range beta-sheet interactions. The peptide is bactericidal against a wide range of pathogenic bacteria in planktonic growth and in biofilms, and reduces bacterial loads in mouse models of *Escherichia coli* and *Acinetobacter baumannii* infections. Our results indicate that disrupting protein homeostasis via co-translational aggregation constitutes a promising strategy for development of broad-spectrum antibacterials.

In recent decades, drug-resistant pathogens have emerged as major global health challenge[1]. These bacteria are notorious for their ability to evade commonly used antibiotics through various multi-drug resistance mechanisms[2,3]. The six most frequently occurring pathogens associated with drug-resistant infections include *Escherichia coli*, *Staphylococcus aureus*, *Klebsiella pneumoniae*, *Streptococcus pneumoniae*, *Acinetobacter baumannii*, and *Pseudomonas aeruginosa*, which were linked to an estimated 3.57 million deaths related to antibiotic resistance in 2019[4,5]. The acronym ESKAPEE (often simplified to ESKAPE) is commonly used to refer to a closely related group of highly virulent and antibiotic-resistant bacterial pathogens that includes all the above, except for *Streptococcus pneumoniae*, and adds

[1]Switch Laboratory, VIB Center for Brain and Disease Research, Leuven, Belgium. [2]Switch Laboratory, Department of Cellular and Molecular Medicine, KU Leuven, Leuven, Belgium. [3]Centre of Microbial and Plant Genetics;KU Leuven, Leuven, Belgium. [4]Center for Microbiology;VIB-KU Leuven, Leuven, Belgium. [5]School of Chemistry, Monash University, Clayton, Vic, Australia. [6]Systems Biology based Mass Spectrometry Laboratory (SyBioMa), KULeuven, Leuven, Belgium. [7]Aelin Therapeutics, Leuven, Belgium. [8]These authors contributed equally: Laleh Khodaparast, Ladan Khodaparast.
✉e-mail: joost.schymkowitz@kuleuven.be; Frederic.rousseau@kuleuven.be

Enterobacter spp. and *Enterococcus faecium*. Given the scale of this threat, new approaches to develop effective antibiotics against these pathogens are urgently needed[3,6].

In this context, antimicrobial peptides (AMPs) are increasingly being explored as promising candidates to combat ESKAPE pathogens[7]. Naturally occurring AMPs are integral components of the innate immune system of many species, including humans, where they play a crucial role in preventing infections[8]. To harness this potential, researchers have developed both natural and synthetic AMPs valued for their fast and efficient bactericidal actvity[7,9]. AMPs are typically short, cationic, amphipathic peptides with variable sequences and structures[8]. Initially, they were regarded as a uniform group of molecules that exert their antimicrobial effects primarily by disrupting bacterial membranes through mechanisms such as pore formation, insertion into the lipid bilayer, disruption of the membrane lipid backbone, or transmembrane channel formation[8]. However, it is now recognized that the mechanism of action of AMPs is more diverse and can also involve interaction with intracellular targets, enhancing their potential as candidate therapeutics against drug-resistant microbes[10]. Interestingly, a subclass of AMPs has been shown to undergo amyloid formation, although the importance of their antimicrobial activity remains unclear[11].

We recently designed antimicrobial peptides with a novel mechanism of action that induces aggregation of a target protein, thereby causing loss of function[12–16]. The mode of action of these peptides is based on aggregation-prone regions (APRs) within their polypeptide sequence, which can drive the misfolding and aggregation of proteins containing homologous APRs[17]. Most proteins have at least one APR in their sequence[18] and targeting can be highly specific. APRs are typically located in the hydrophobic core of globular proteins or in transmembrane (TM) regions of TM proteins[18], which are sites where mutation rates are intrinsically low. For instance, peptides designed to target beta-lactamases exhibit a knock-out phenotype, meaning they show conditional toxicity in the presence of beta-lactam antibiotics[12]. These peptides can even differentiate between related classes of beta-lactamases whose APRs differ by a few amino acids.

An alternative design principle for antibacterial aggregating peptides is to find APRs that occur in multiple proteins within the bacterial proteome[14], thereby targeting a broader range of proteins simultaneously. This strategy aims to reduce the impact of single resistance-conferring mutations[19] and cause widespread aggregation, leading to proteostatic collapse. Given the known value of bacterial membrane homeostasis as a target for broad spectrum antibiotics, we explored whether disruption of membrane protein folding could yield broad-spectrum antibacterial activity against ESKAPE pathogens. For this purpose, we turned to a peptide called P33 that we previously identified in a screen against *E. coli* using randomly selected APRs of *E. coli* proteins[14]. The screen was designed to select APRs that have a maximal number of homologous fragments occurring in different proteins across the *E. coli* proteome, with the goal of inducing the aggregation of multiple proteins at once and causing a failure of protein homeostasis[14]. P33 emerged as a potent hit and is based on an APR from the transmembrane region of *E. coli* threonine/homoserine exporter RhtA (UniProt identifier RHTA_ECOLI, Fig. 1A). The peptide follows our typical design pattern, consisting of a tandem repeat of an APR of RhtA ($_{97}$LGIAVAL$_{103}$,), flanked by arginine residues and separated by a linker (to yield R-LGIAVAL-RR-P-R-LGIAVAL-RR, Fig. 1A). The arginine residues are known to be critical for bacterial cell uptake and hence the overall antibiotic effect[19]. This profile of hydrophobic peptides with a positive charge is also seen in 'classical' AMPs that act directly on the membrane[8]. In a subsequent study on resistance development in *E. coli*, we observed a lack of resistance build-up against this peptide, including in the hypermutating *E. coli* strain XL-1 Red[19], consistent with a mode of action involving multiple targets.

In the current study, we focused on the mode of action and broad-spectrum activity of P33 and discovered it causes aggregation of many proteins, with a bias towards transmembrane proteins and ribosomal components. Given the importance of this type of proteins as drug targets in broad-spectrum antibiotics, we screened for activity against other ESKAPE pathogens in which the targets are conserved and found broad-spectrum activity of our peptide, with a conserved mode of action across the tested spectrum. Although these linear hydrophobic peptides are challenging drug candidates, we obtained encouraging results in models of urinary tract infection and sepsis.

Results

The mode of action of P33 depends on protein aggregation

Here, we first wanted to confirm the efficacy of P33 against *E. coli* and establish whether its effect indeed involves intracellular aggregation. In *E. coli*, aggregation typically results in the formation of polar inclusion bodies (IBs). To reveal these, we turned to super resolution structured illumination microscopy (SIM) of *E. coli* ATCC 25922 cells stained with pentameric formyl thiophene acetic acid[20] (pFTAA, commercially known as Amytracker). This dye becomes strongly fluorescent upon binding to amyloid-like aggregates and is widely used to study aggregation. Thus, if cells display IBs that are positive for pFTAA, this is a strong indication that intracellular aggregation occurs. As negative controls, we studied bacteria that were treated with the beta-lactam antibiotic ampicillin (Fig. 1B) or the classic membrane-disrupting polymyxin antibiotic colistin (Fig. 1C), neither of which revealed pFTAA-positive IBs. Bacteria treated with P33 however, showed the typical inclusion bodies occupying a significant fraction of the cell (Fig. 1D, E), confirming that intracellular aggregation occurs upon this treatment. As a positive control, we compared these stainings to heat shock and overexpression of the highly aggregation-prone DNA-binding domain of p53[21] and to alternative amyloid-aggregation dyes Thioflavin-T and HS-169 (Supplementary Fig. 1). To confirm the amyloid-like nature of these inclusion bodies using a label-free technique, we performed Atomic Force Microscopy-based Infrared Spectroscopy (AFM-IR), which allows for an analysis of the secondary structure content of protein-containing samples from the infrared absorption spectrum, at the spatial resolution of the AFM. To achieve this, we embedded bacteria in resin, cut ultra-thin sections and analyzed these with the AFM-IR, to get single-cell maps of secondary structure content, as previously described[22]. This revealed regions at the cell poles of high protein concentration (Fig. 1F) and enriched in beta-sheets (seen as a shoulder at 1630 cm^{-1} in Fig. 1G), again consistent with the typical nature of inclusion bodies.

To assess if the peptide produces obvious damage to the cell membrane in that time frame, we turned to Scanning Electron Microscopy (SEM) of treated cells and found no overt signs of membrane damage in the vehicle-treated (Fig. 1H) or P33 treated (Fig. 1I) samples. Similar observations were made using Transmission Electron Microscopy (TEM) of ultrathin sections of resin-embedded bacteria (Supplementary Fig. 2). These results are consistent with a primarily intracellular mode of action. As a positive control, we could detect typical membrane damage patterns with the control treatment with colistin (Fig. 1J and Supplementary Fig. 2). To investigate this further, we utilized Quartz Crystal Microbalance with dissipation monitoring (QCM-D), a biophysical technique known for accurately revealing AMP-lipid bilayer interactions[23–25]. We introduced P33 at concentrations of 1, 10 and 50 μM to POPC:POPG (4:1) lipid bilayers on the QCM-D sensor (Supplementary Figs. 3 & 4). At all tested concentrations, the peptide did not show significant binding to the bilayer ($\Delta f < 0.5$ Hz) and no structural change in the lipid bilayer were observed ($\Delta D \sim 0$). Interestingly, during the introduction of the P33 into the chamber (sensor + lipid), a very small binding 'insertion' was noted at 10 and 50 μM ($\Delta f < 0.5$ Hz) and once the flow ceased, the peptide was excluded (eliminated) from the lipid bilayer. This is similar to QCM-D data for

https://doi.org/10.1038/s41467-025-56873-z

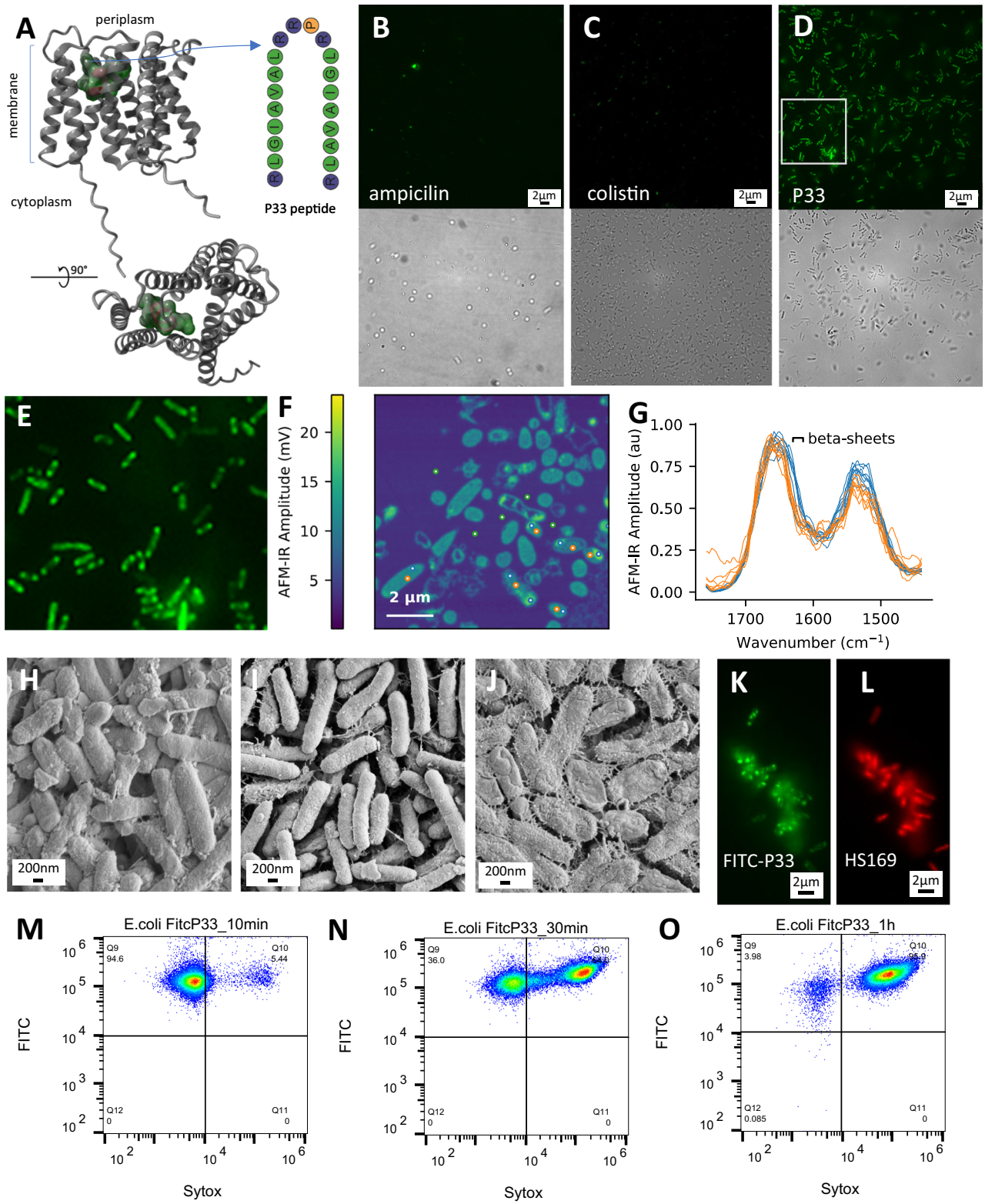

proline-rich -AMPs that were obtained earlier[25] and also reminiscent to the behavior of the Tat peptide at a DMPC:cholesterol bilayer[23]. These data contrast the mode of action observed for lytic (frog derived) AMPs investigated using QCM-D[26,27], thus showing that the P33 peptide is capable of traversing the membrane without any structural impact on the lipids and can enter the bacteria capable of binding intracellular targets.

We then turned to a fluorescent derivative of P33 (FITC-P33), which retained the antibacterial activity (MBC and MIC) of the parent molecule (Table 1). When we performed SIM fluorescent microscopy using FITC-P33 and a red-shifted version of pFTAA named HS169[28], we also observed a similar pattern of intracellular IBs (Fig. 1K, L). This showed that part of the IBs consisted of the peptide, but also that there is no major accumulation of the peptide in or at the membrane. Moreover, this allowed us to further study the process using Fluorescent Activated Cell-Sorting (FACS) with a two-color readout: monitoring peptide uptake using FITC, intracellular aggregation using HS169 and cell death using the Sytox Blue nucleic acid stain, which

Fig. 1 | The mechanism of action of P33 is dependent on protein aggregation. **A** Structural views of the RhtA protein image generated with Yasara. The peptide P33 is derived from an APR sequence of the *E. coli* threonine/homoserine exporter RhtA (left). The peptide is designed according to the standard pattern, which consists of an APR of RhtA ($L_{97}GIAVAL_{103}$) repeated in tandem, flanked by arginine residues and separated by a linker (right). Super resolution structured illumination microscopy (SIM) of *E. coli* ATCC 25922 cells stained with pFTAA upon treatment with **(B)** the beta-lactam antibiotic Ampicillin, **(C)** the classic membrane disrupting polymyxin antibiotic colistin, or **(D, E)** P33. Images show a single representative micrograph of one out of three independent repeats performed. **F** Atomic force microscopy-based infrared spectroscopy (AFM-IR) image of *E. coli* ATC 15922 treated with P33, highlighting inclusion body (blue), cytoplasm (orange) and epoxy (green) spectra indicated. The experiment was independently repeated three times with similar results. **G** Normalized AFM-IR spectra from locations indicated in (F). The inclusion body spectra exhibit a shoulder at 1630 cm-1, indicative of amyloid formation. Scanning Electron Microscopy (SEM) image of *E.coli* cells treated with **(H)** the vehicle control **(I)** P33 or **(J)** colistin. The experiments were conducted independently on three separate trials. **K, L** SIM microscopy of *E. coli* cells treated with FITC-P33 (K, green channel) and stained with the amyloid dye HS169, a red-shifted version of pFTAA (L, red channel). Fluorescence-activated cell sorting (FACS) analysis of 40,000 *E. coli* cells, treated with FITC-P33 for 10 minutes **(M)**, 30 minutes **(N)** and 1 hour **(O)**. Cells were stained with Sytox for viability assessment and HS169 to monitor aggregation simultaneously.

Table 1 | Minimum inhibitory concentration (MIC) and Minimum bactericidal concentration (MBC) of P33 against various bacterial strains

		P33	
Microorganisms	**Bacterial strains**	**MIC (μg/ml)**	**MBC (μg/ml)**
Gram-negative bacteria	*Escherichia coli ATCC25922*	3	3
	Acinetobacter baumannii ATCC 19606	6	6
	Pseudomonas aeruginosa ATCC	6	6
	Klebsiella pneumoniae ATCC 13883	16	16
	Enterobacter cloacae ATCC 13047	16	16
	Salmonella typhimurium EKE 1999	16	16
Gram-positive bacteria	*Staphylococcus aureus MRSA ATCC 25213*	16	16
	Staphylococcus epidermidis	8	8
	Enterococcus faecium ATCC 29212	*16*	*16*

enters cells only upon permeabilization. The FACS analysis of P33-treated cells showed that peptide uptake precedes massive permeabilization of the membrane to the Sytox Blue dye (indicative of cell death), indicating that peptide uptake does not require massive disruption of membrane integrity, consistent with a mode of action that initiates intracellularly (Fig. 1M–O). Aggregation and cell permeabilization to Sytox Blue appear to occur at similar rates, after peptide uptake (Supplementary Fig. 5). Control experiments with vehicle or heat treated (95 °C) cells are provided in Supplementary Fig. 6.

P33 has a broad spectrum of activity

To evaluate the potential broad-spectrum potential of the P33 peptide, assuming it works by engaging homologous sequences in other proteins through co-aggregation, we analyzed the distribution of BLOSUM80 scores of homologous sequence matches to the P33 APR across the *E. coli* proteome, allowing up to 3 mismatches, and compared it to the distribution obtained with 10 random peptides of the same length (Fig. 2A). We then calculated what fraction of the distribution corresponded to high similarity scores (BLOSUM80 score > 60% of the self-match score), and we observed that there are about twice as many matches for the P33 APR as for the random sequences (Fig. 2B). Since the same enrichment of sequence matches was observed for many other ESKAPE proteomes (Fig. 2A–C), we reasoned that P33 could have broad-spectrum activity against the full ESKAPE range, provided that peptide uptake was sufficiently efficient in all strains. Indeed, the number of high similarity matches in these proteomes ranges from 3 in *E. cloacae* to 17 in *K. pneumoniae* (Fig. 2C). Clustering analysis of the proteins that contain these sequence matches showed that, although some of the matches occur in orthologous clusters, the majority occur in unrelated proteins in each species (Supplementary Fig. 7A), and the sequence pattern in these matches is strongly conserved (Supplementary Fig. 7B). Gene Ontology term enrichment analysis of these proteins does show however that these matches are strongly biased towards membrane proteins, as could be expected for an APR that originates in a transmembrane helix (Supplementary Fig. 7C). Many of the potential sequence matches of P33 are involved in some form of membrane transport.

We thus set out to examine the antimicrobial activity of P33 against a diverse set of multidrug-resistant (MDR) gram-positive and gram-negative bacterial strains, using the microdilution assay. The species included *Acinetobacter baumannii, Pseudomonas aeruginosa, Klebsiella pneumoniae, Enterobacter cloacae, Salmonella typhirium*, Meticilline-resistente *Staphylococcus aureus* (MRSA), *Staphylococcus epidermidis*, and *Enterococcus faecium* and the resistance profile of the strains used is summarized in Suppl. Table 1. P33 exhibited a potent broad-spectrum antibacterial activity against most tested bacterial strains (Table 1) and the MIC and MBC concentrations were closely matched, indicating a bactericidal mode of action. Next, we moved to screen a larger collection of 132 clinical isolates from 6 species, collected from a range of countries and affected organs (Suppl. Table 2 and Fig. 2D) and we found both susceptible and resistant clones for each species, except MRSA, which showed a relative resistance. These results suggest that the multi-target mode of action of P33 may protect it from resistance through target modification by mutation, but it remains susceptible to acquisition of resistance genes (like efflux pumps or proteases, e.g.) through horizontal gene transfer[29,30].

Finally, we also checked if the peptide retained its activity against *E. coli* (K-12 BW25113), *Staphylococcus aureus* (ATCC 83254) and *Pseudomonas aeruginosa* (ATCC 27853), growing in a biofilm, which has clinical relevance[31]. To this end, we allowed biofilm attachment in 96-well plates and employed crystal violet staining to quantify the amount of biofilm formed in the presence and absence of peptides after 24 hours (Fig. 2E). This revealed a clear reduction in the amount of biofilm formed at concentrations close to the MIC values, showing that P33 is active in both planktonic and biofilm bacteria (Fig. 2F).

To confirm that widespread protein aggregation in the bacterial cells is indeed part of the antibacterial mode of action of P33 in all the strains studied, we performed super-resolution structured illumination microscopy (SIM) of diverse bacterial strains treated for 1 hour at MIC concentration with P33 and stained with pFTAA, as before

https://doi.org/10.1038/s41467-025-56873-z

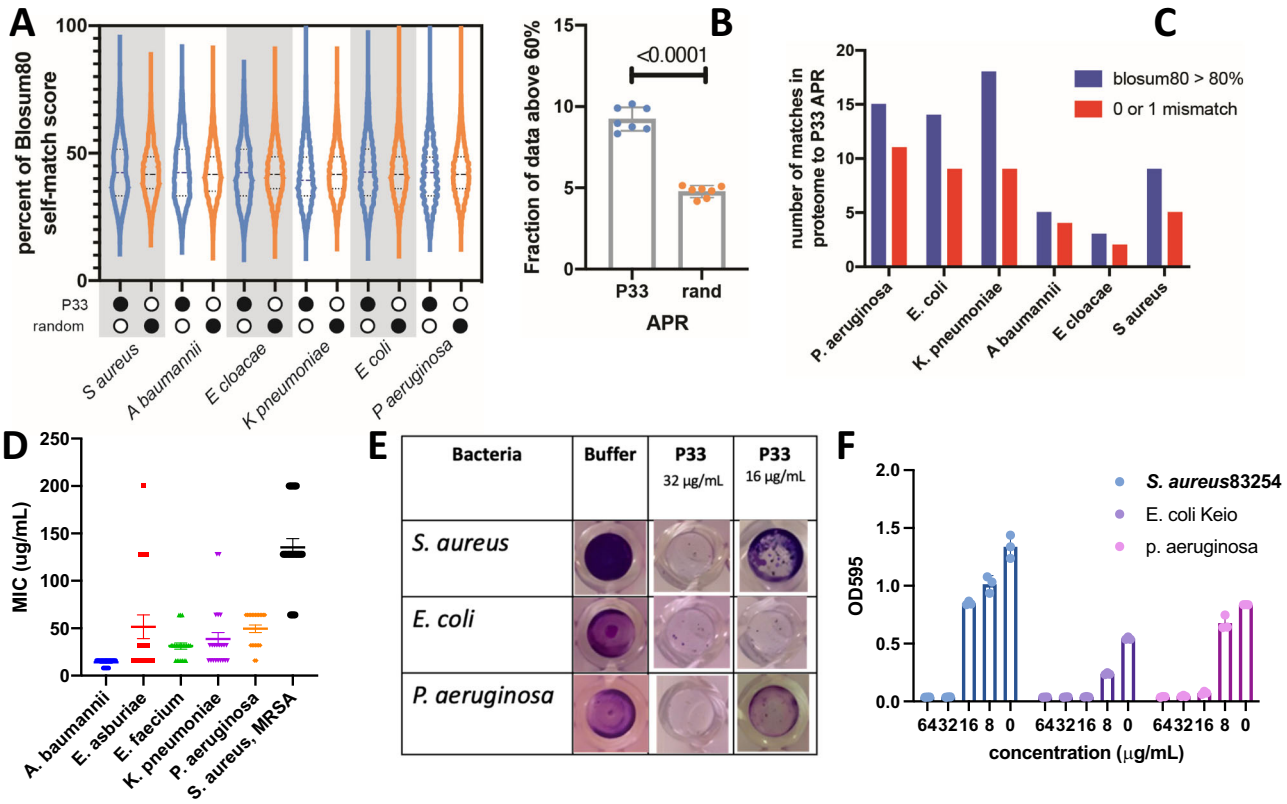

Fig. 2 | Broad spectrum activity of P33 peptides. A Distribution of the BLOSUM80 scores of homologous sequences matching the P33 APR across the *E. coli* proteome, compared to the distribution obtained with 10 random peptides of the same length. **B** Fraction of scores in its distribution corresponding to high similarity scores (BLOSUM80 score > 60% of the self-match score). The data are represented as mean ± S.D., student t-test was used for statistical analysis. **C** Number of high similarities matches of the P33 APR in the full proteome panels of ESKAPE pathogens. The plot represents the exact number of matches with the indicated properties. **D** Minimum inhibitory concertation (MIC) value of P33 against 132 clinical isolates from six different bacterial species. The plot shows all the data points, as well as the mean and standard deviation. **E**, **F** Effect of P33 peptides on biofilm formation in strains of *S. aureus*, *E. coli*, and *P. aeruginosa*. Data represent the average and standard deviation of three independent biological replicates ($n = 3$), each derived from different experimental units (separate bacterial cultures). The unit of study is the independent bacterial culture, which was assigned a specific treatment condition. Error bars represent the standard deviation across these biological replicates. Control groups, where applicable, are explicitly defined as the buffer-treated samples.

(Fig. 3A). In all tested strains, the SIM micrographs revealed the presence of polar inclusion bodies, the well-known hallmark of protein aggregation in bacterial cells. SEM imaging of the cell membranes again revealed no major abnormalities in any of the strains tested, suggesting that the main mode of action is intracellular (Fig. 3B–D). Analysis of the time of killing of the bacteria revealed that P33 reduces viability of the cultures to below 20% in 1 to 4.5 hours, depending on the species (Fig. 3E). This rate of killing correlated with the fraction of aggregation-positive cells, as determined by Amytracker staining and FACS analysis (Fig. 3F, G and Supplementary Fig. 8). Together these results show that the aggregation-based mode of action of P33, by inducing widespread aggregation, is conserved across a wide spectrum of bacterial strains.

P33 induces protein aggregation of many bacterial proteins

The data so far leave unanswered the question of whether the IBs consist only of the peptide or if bacterial proteins are also involved. There are well-established protocols for the specific extraction of proteins trapped in IBs, particularly in *E. coli*[32] (Supplementary Fig. 9). We performed IB extractions of various strains such as *E. coli* ATCC 25922, *S. aureus* MRSA ATCC 25213, *S. epidermidis*, *P. aeruginosa* ATCC 27853, *E. cloacae*, *K. pneumoniae* ATCC 13883, and *A. baumannii*, ATCC 19606 treated for 1 h with P33 when aggregation is already widespread and subjected them to SDS-PAGE (Fig. 4A). This revealed that bacterial proteins of various sizes are indeed in the IB fraction, whereas this is not the case in untreated cells.

We then analyzed the samples of *E. coli* (ATCC 25922) by mass-spectrometry-based (MS) proteomics to compare protein abundances between the soluble and IB fraction of P33 treated cells. To elucidate the dynamics of IB formation, the IB fraction was collected at several time points: immediately after treatment (0 minutes), as well as at 5, 10, 20, 40, and 60 minutes. On the other hand, the soluble fraction was collected at time points 0 and 60 minutes. Importantly, the same number of bacterial cells was used across all time points, allowing a detailed observation of IB formation over time. We reliably detected 1188 proteins in the soluble and IB fraction across all time points, confirming that P33 treatment causes aggregation of many bacterial proteins into IBs. Notably, protein abundance in the IB fraction grows over time, further indicating that P33 effectively induces protein aggregation (Fig. 4B). Comparative analysis of the normalized protein composition between the soluble and IB fractions after 1 hour revealed that 120 proteins were significantly enriched in the IB fraction ($\log_2$ Fold Change >= 1 and adjusted p-value <= 0.05) (Fig. 4C). Gene Ontology enrichment analysis of these proteins showed strong enrichment of outer membrane proteins (Fig. 4D), consistent with the origin of the P33 sequence from a transmembrane segment. In fact, the Outer Membrane Protein A (OmpA), which has a region with high local homology (BLOSUM80 score = 73%) to the APR of P33, is the fourth most abundant protein enriched in the IB fraction (Fig. 4E). Notably, the Gene Ontology enrichment analysis also pointed to proteins involved in protein translation, including many ribosomal components (Fig. 4D), such as the 50S ribosomal protein L23 (RplW; Fig. 4F). This

https://doi.org/10.1038/s41467-025-56873-z

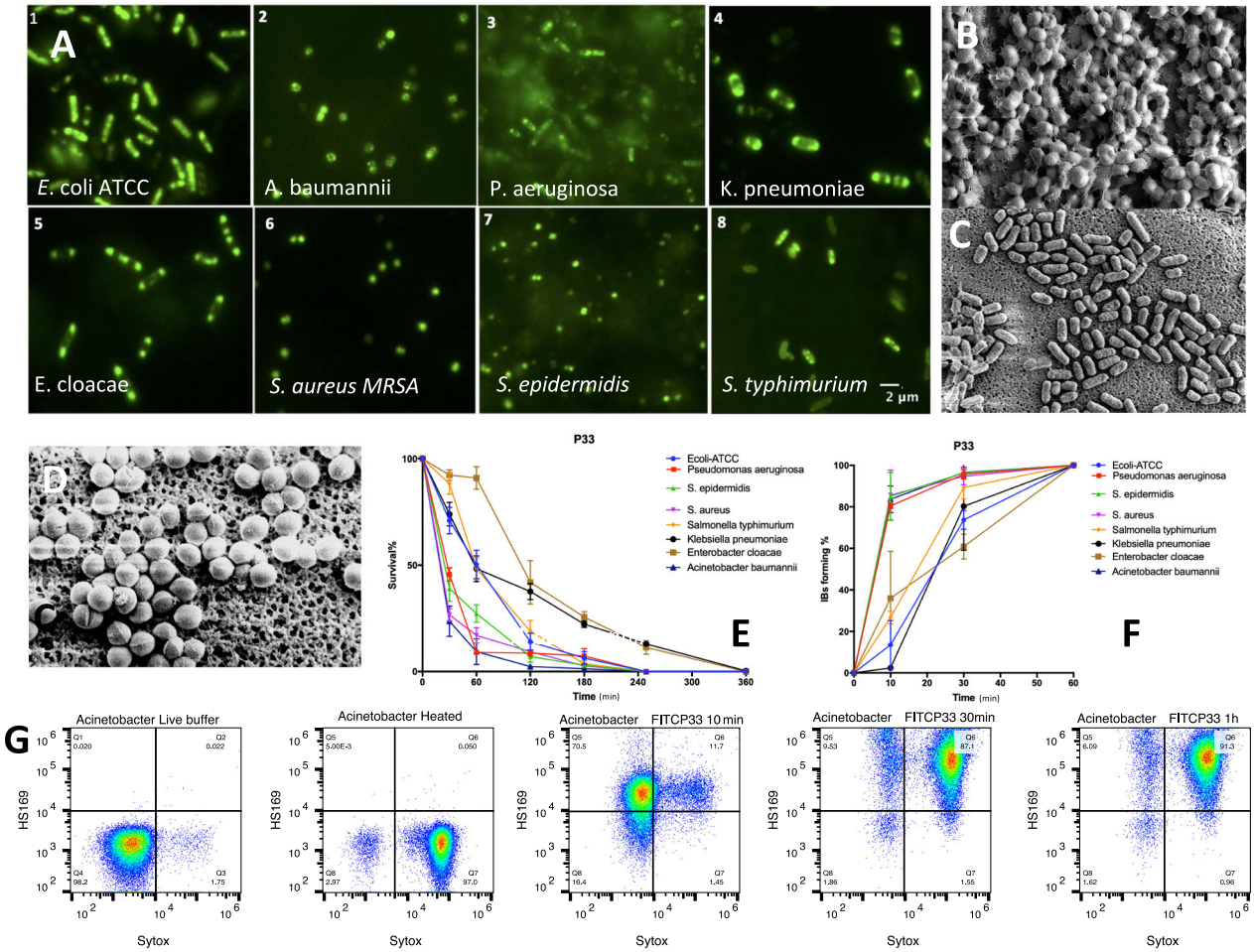

Fig. 3 | Induction of aggregation in cells upon P33 treatments. A Structured illumination microscopy (SIM) images of bacterial strains treated with P33 at the MIC concentration and stained with the amyloid-specific dye pFTAA (0.5 μM). **B**–**D** Scanning electron microscope (SEM) images of bacteria (*Acinetobacter* baumannii ATCC 19606), *E. coli* ATCC25922 and *Staphylococcus* aureus ATCC 25213) treated by P33 showing no adverse effect on the cell membrane. **E** Time-killing curve of P33 against various bacterial strains treated at MIC concentration. Data represent the average and standard deviation of three replicates. **F** Time-dependent fraction of aggregation-positive cells, determined by pFTAA staining and FACS analysis. Data represent the average and standard deviation (SD) of three biological replicates (each with independent experimental units). Error bars represent the standard deviation (SD) of the mean for each data point. **G** Fluorescence-activated cell sorting (FACS) analysis of 40,000 *Acinetobacter* baumannii ATCC 19606 cells, measuring FITC fluorescence as peptide uptake, Sytox as a dead cell identification, and HS169 for aggregation detection, treated at MIC concentration for 10 minutes, 30 minute and 1 hour. Controls include live and heat-inactivated cultures. Data shown are from a single replicate of one of three independent experiments.

suggests that aggregation induction by this peptide may occur co-translationally, aligning with previous reports of similar behavior observed with a different peptide[14]. No enrichment of GO terms related to biological processes or molecular functions was detected, implying that P33 treatment does not perturb specific cellular processes. Analysis of the biophysical properties of the aggregates revealed significantly larger isoelectric points of the enriched proteins, attributable to a higher net positive charge (Supplementary Fig. 10A-D). This difference is primarily driven by the enrichment of ribosomal proteins in the IB fraction, as it disappears upon removal of these proteins (Supplementary Fig. 10E). The intended mode of action of P33 is to drive the aggregation of proteins with high local homology to its sequence. The *E. coli* proteome has 34 proteins with very high local homology (BLOSUM80 score > 70%) to the APR of P33 (Table 2). However, out of these proteins, only five are detected in the MS, three of them being enriched in IBs: OmpA, the Translocation and assembly module subunit TamA (TamA) and Long-chain fatty acid transport protein (FadL). Analysis of the biophysical properties of these 34 proteins revealed that the three enriched proteins—OmpA, TamA, and FadL—have the highest percentage of beta-sheet content (Fig. 4G), which tends to come with more long-range interactions and less efficient folding than the alpha-helical proteins that do not appear to be targeted[33–35]. So, our data do not unequivocally demonstrate a sequence-based targeting, and the induction of aggregation may instead be caused by more general properties, but it does appear to be associated to membrane proteins.

Next, we looked at the changes in IB composition over time, particularly, of proteins whose proportion increases as the IBs form. To this end, we normalized the protein abundance values of the IB fraction across all time points and conducted a linear regression analysis. Among the top 50 proteins exhibiting the highest increase in slope, only 12 were found to be significantly enriched in the IBs compared to the soluble fraction (Fig. 4H). Notably most ribosomal and outer membrane proteins, such as OmpA and RplW, did not increase in proportion as the IBs formed (Supplementary Fig. 11A, B). This observation indicates that these proteins accumulate at the same rate as the IBs, suggesting either that P33 induced aggregation occurs very rapidly (within seconds) or that a basal level of proteins that are continuously aggregated exists, which is exacerbated after P33 treatment. Interestingly, among the proteins with the highest proportional

https://doi.org/10.1038/s41467-025-56873-z

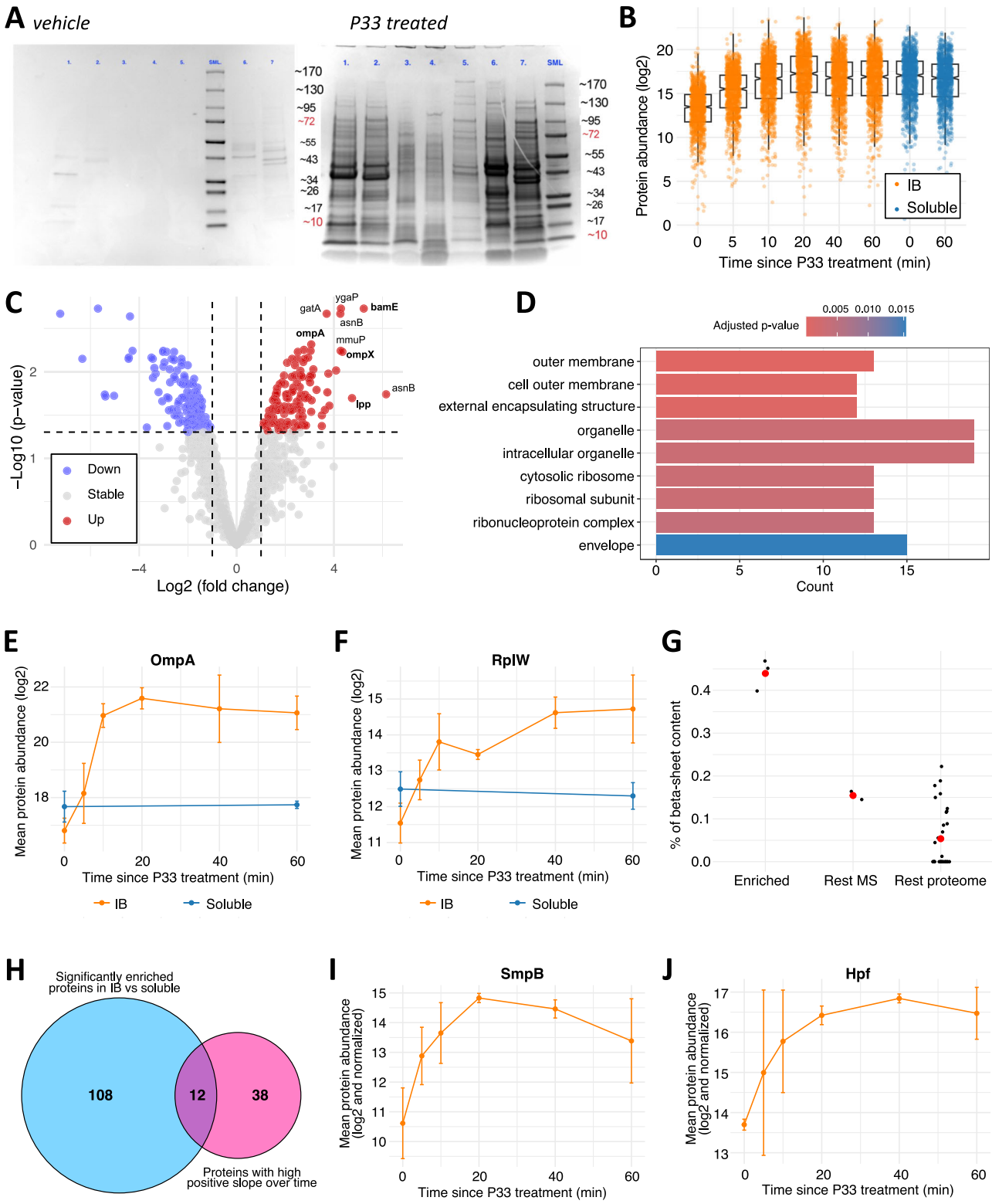

increase, we identified two ribosome rescue factors: Ssra-binding protein (SmpB) and ribosome hibernation promoting factor (Hpf) (Fig. 4I, J). Moreover, we identified other proteins involved in translation regulation, such as RNA-binding protein Hfq (Hfq), and several chaperones, including J domain-containing protein DjlB (DjlB). This data points to a scenario in which the potential targets of P33 accumulate at a constant rate within the IBs, while several regulatory proteins are actively recruited as part of the cellular response to manage IB formation.

RNA sequencing of inclusion bodies points towards ribosome stalling and nascent chain-mediated aggregation

The enrichment of ribosomal proteins and the activation of ribosome rescue factors as the IBs form suggest that stalled ribosomes might be trapped within IBs. Staining of treated bacteria with SYTO RNASelect Green Fluorescent Cell Stain (Invitrogen) revealed a pattern of RNA accumulation in inclusion bodies (Fig. 5A). Encouraged by this, we performed RNA extraction on the inclusion body fraction of treated bacteria after 1 h. Analysis using capillary electrophoresis revealed 30S

Fig. 4 | Inclusion bodies composition points to co-translational proteostatic collapse. A Representative Coomassie blue-stained SDS-PAGE of inclusion body extractions from various strains treated with vehicle (left) or P33 (right) at MIC concentration for one hour in *E. coli* (Lane 1), *Staphylococcus aureus* MRSA (Lane 2), *Staphylococcus epidermidis* (Lane 3), *Pseudomonas aeruginosa* ATCC 19606 (Lane 4), *Enterobacter cloacae* ATCC 13047 (Lane 5), *Klebsiella pneumoniae* ATCC 13883 (Lane 6) and *Acinetobacter baumannii* ATCC 19606 (Lane 7). The molecular-weight marker is shown in lanes 8. **B** Protein abundances (log_2) in the soluble and IB fractions of P33-treated cells by mass-spectrometry at different time points. The box spans the interquartile range (25th to 75th percentiles), the line inside the box represents the median, and the whiskers extend to the minimum and maximum values within 1.5 times the interquartile range. The notch around the median indicates an approximate 95% confidence interval. **C** Volcano plot illustrating the differences between the soluble and IB fraction after 1 h. Up: proteins significantly upregulated in the IBs fraction (log_2 Fold Change >= 1 and adjusted *p*-value <= 0.05). Down: protein significantly downregulated in the IBs fraction (log_2 Fold Change <= 1 and adjusted *p*-value <= 0.05). Log_2-transformed and quantile-normalized protein abundances were analyzed using linear modeling and moderated t-tests (limma). Adjusted p-values were calculated using the Benjamini-Hochberg method to control the false discovery rate. **D** Gene Ontology (GO) enrichment analysis of the proteins enriched in inclusion bodies. GO terms across all three ontologies were tested for enrichment using a hypergeometric test, with Benjamini-Hochberg correction (adjusted *p*-value < 0.05). Redundant terms were simplified by clustering based on semantic similarity (cutoff = 0.7), retaining the most significant term per cluster. OmpA (E) and RplW (F) abundance over time in the soluble and IB fraction after treatment with p33. The line represents the average value at each position (log_2), while the error bars indicate the standard deviation. **G** Percentage of beta-sheet propensity for proteins containing a region with high local homology to the APR of p33. Red dots indicate the average value in a group. **H** Overlap between significantly enriched proteins in the IB fraction vs soluble after 1 h and proteins with highest proportional increase in the IB fraction over time. SmpB (I) and Hpf (J) normalized abundance over time in IB fraction after treatment with p33. The line represents the average value at each position (log_2), while the error bars indicate the standard deviation.

and 50S ribosomal RNA in these extracts, as well as shorter species, likely mRNA (Fig. 5B). We then proceeded to deplete the ribosomal RNA from the samples to characterize the other species using RNA sequencing (Illumina MiSeq). This method detected 4052 mRNA species across the IB fraction. Of the 1188 proteins detected in the IB fraction by MS, 94.9% were found in the RNAseq data. Initial comparisons between protein abundance in the IB fraction by MS with the mRNA abundance in the same fraction showed a weak correlation (Pearson correlation of 0.1, p-value < 0.001). However, this discrepancy may arise due to the higher sensitivity and sequencing depth of RNAseq compared to MS. To investigate this further, we sorted the MS data by protein abundance and divided it into equal bins. Notably, bins with higher protein abundance showed a larger presence of the most highly expressed mRNAs (Fig. 5C), indicating that the two values are correlated. Together, this suggests that translating ribosomes containing both mRNA and protein may be trapped in the inclusion bodies. To confirm this hypothesis, we studied the bactericidal effect of P33 on *E. coli* ATCC 25922 in the presence of the bacteriostatic macrolide antibiotic erythromycin, which binds near the nascent chain exit channel of the ribosome, thereby inhibiting protein translation, although the exact mode of action remains unclear[36]. In line with a co-translational mode of action, inhibition of the ribosome with 100 µg/mL of erythromycin rescued the viability of *E. coli* in the presence of otherwise lethal doses of P33 (Fig. 5D), which was accompanied by a drop in pFTAA staining compared to P33 treatment alone (Fig. 5E). These results show that active protein translation is required to mediate the antibacterial effect of P33. To exclude the possibility that P33 acts directly on the ribosome, thereby causing stalling independently of the nature of the nascent chain, we turned to the PURE Express in vitro translation system. We provided mRNA encoding GFP and exposed the reaction mixture to a concentration range of P33. The resulting GFP fluorescence (Supplementary Fig. 12) shows that the amount of GFP produced in this setting is not affected by the presence of P33, suggesting that the peptide exerts no direct action on the ribosome independent of the transcript and in addition, that it also does not act on the GFP transcript.

The MS proteomics data above revealed that SmpB is recruited to IBs after P33 treatment. Notably, analysis of the RNA sequencing data revealed that transfer-messenger RNA (tmRNA), also known as *SsrA*, is one of the most abundant RNA species found in the IB fraction (6th out of 4070). The SmpB-tmRNA/*Ssra* complex is the main ribosome rescue system in bacteria by tagging nascent chains on stalled ribosomes for proteolysis[37]. In line with this, several proteases that have been shown to recognize and degrade *SsrA*-tagged nascent chains, such as ClpXP, ClpAP, and Lon[38], were also present in IBs after P33 treatment based on the MS data, although they were not enriched. Together, these findings suggest that ribosome rescue mechanisms are activated before bacterial cell death occurs, although it remains unclear why exactly it does not resolve the toxicity. To investigate this further, we used CRISPR-based genome editing to create a reporter strain (based on *E. coli* BW25113) in which the peptide tag that is endogenously added to the C-terminal of stalled nascent chains during *SsrA*-based ribosome rescue, is replaced by an HA-tag (Supplementary Fig. 13). So, in this engineered strain, when ribosome-stalling occurs, the nascent chains on the ribosome at the time of stalling will be aborted and labeled with an HA-tag, which can be easily detected using antibodies. Western blot analysis of P33-treated bacteria revealed abundant accumulation of HA-tagged polypeptides across the molecular weight range of the gel, which did not occur in vehicle-treated samples (Fig. 5F & G). Within the P33-treated sample, the HA-tagged species were enriched in the IB fraction, which, together with the previous data, indicates that ribosome rescue mechanisms are activated and that nascent chains are tagged in a co-translational fashion in response to P33 treatment. This implies that IBs likely contain stalled ribosomes, stalled nascent chains, and their cognate mRNAs. The presence of other ribosome rescue factors in the IBs, such as Hpf, suggests that other translation stress responses might be activated. Nevertheless, neither the Alternative ribosome rescue factor A (ArfA) nor the Alternative ribosome rescue factor B (ArfB) were detected in our dataset.

Taken together, our data point towards the aggregation of nascent chains during translation after P33 treatment, which leads to ribosome stalling and proteostatic collapse. As a final test of this hypothesis, we created an artificial construct that recreates our hypothesized situation of a ribosome that is stalled with the nascent chain exposing an APR. To ensure this, we separated an amino-terminal APR from a carboxy-terminal ribosomal stall (poly-lysine) site with a linker that is sufficiently long to allow the APR to emerge from the ribosome before the stall-site is reached. We added a C-terminal GFP to the construct to detect full-length constructs, resulting from read-through of the stall site (Fig. 5H). As the APR, we used a segment of beta-galactosidase that we have studied extensively before and which is known to produce aggregates in *E. coli*[39,40]. Inspection of bacteria expressing this construct by microscopy shows weak, diffuse GFP fluorescence, suggesting that a small amount of full-length construct is being made (Fig. 5I). However, the phase contrast images show clear inclusion bodies that are not visible in the fluorescence image, consistent with IBs containing stalled nascent chains (Fig. 5J). A construct with a mutationally suppressed APR did not show such IBs, confirming the APR is needed for this effect. To determine whether the observed effects were due to ribosome stalling rather than GFP misfolding, we performed a western blot analysis (Fig. 5K), which confirmed the production of full-length GFP in the construct with the mutationally suppressed APR, but not in the construct with the intact APR. Also, a construct with the APR, but not the staller site showed no inclusions

Table 2 | *E. coli* proteins with high local homology to the APR of P33 (proteome level)

UniProt ID	Gene name	Fold change	Norm.Blos.80	Is it an outer membrane protein?
P0A910	ompA	3.06	72.73	Yes
P0ADE4	tamA	1.95	75.76	Yes
P10384	fadL	1.22	75.76	Yes
P33363	bglx	-1.01	78.79	No
P77488	dxs	-3.37	72.73	No
P0AA67	rthA	Not detected	100	No
P16701	cysU	Not detected	93.94	No
P75797	gsiB	Not detected	87.88	No
P31680	djlA	Not detected	84.85	No
P23890	cadC	Not detected	81.82	No
P76350	shiA	Not detected	81.82	No
P0AFR7	ycjO	Not detected	81.82	No
P0ADR2	ygdD	Not detected	81.82	No
P27842	yigF	Not detected	81.82	No
P63264	cbpM	Not detected	78.79	Yes
P11072	lit	Not detected	78.79	No
P0AEX7	livH	Not detected	78.79	No
P0A769	mntH	Not detected	78.79	No
P0A6W3	mraY	Not detected	78.79	No
P0AGH8	pstC	Not detected	78.79	No
P0AA67	rhtA	Not detected	78.79	No
P10906	ugpE	Not detected	78.79	No
P76419	yegV	Not detected	78.79	No
P37642	yhjD	Not detected	78.79	No
Q46831	yqgA	Not detected	78.79	No
P0AE24	araE	Not detected	75.76	No
P37637	mdtF	Not detected	75.76	No
P69212	mdtJ	Not detected	75.76	No
P41052	mltB	Not detected	75.76	No
P0AEC5	barA	Not detected	72.73	No
P0AAG5	mdlB	Not detected	72.73	No
P37760	rfbD	Not detected	72.73	No
P27125	rhaT	Not detected	72.73	No
P0AGF6	tdcB	Not detected	72.73	No
P32129	yihG	Not detected	72.73	No

Proteins that are detected in the MS following P33 treatment are indicated.

and diffuse GFP expression. These findings suggest a co-translational model of action that relies on the exposure of APRs in the nascent chain.

Evaluation of in vivo efficacy

We wondered if the peptide could display an antibacterial effect in vivo. To prepare for such experiments, we first evaluated the potential toxicity of P33 to primary human erythrocytes and human cell lines, which revealed no strong toxicity (Fig. 6A, B). In initial dose escalation tests with intravenous administration of P33 in C57BL/6Jax mice, we observed tolerability issues from 1 mg/kg administered dose, which is known to occur for hydrophobic and positively charged peptides. However, we noted a strong mitigating effect with FITC-P33.

Two murine infection models were employed in this study, a bacterial urinary tract infection (UTI) model and a sepsis model. In the UTI model, we used a catheter to infect the urethra of female C57BL/6JAX mice (8-10 weeks) with an inoculum containing 10^6 cells of *E. coli* strain ATCC 25922. At 1-hour post-inoculation, the mice received 10 mg/kg of FITC-P33 administered intravenously. Ampicillin was used as a control (30 mg/kg) and was administrated orally. After 24 hours the mice were sacrificed, and the bacterial load in the bladder, ureter, kidney, liver, and spleen was quantified by determining the number of Colony Forming Units (CFU) per mL of extracted tissue (Fig. 6C–G). Results showed a reduction of 2-3 log-fold in bacterial load in the urinary tract organs in vivo. The second experiment was a septicemia murine model in which we infected mice with *A. baumanni* ATCC 19606 via intraperitoneal injection. Treatments were administered 1 hour and 3 hours post-infection and consisted of FITC-P33 (10 mg/kg, subcutaneously), vehicle or Tigecycline (30 mg/kg, subcutaneously). Blood was collected 24 hours post-infection for CFU counting to quantify the number of viable bacteria (Fig. 6H). In this setup, the peptide achieved a single log-fold reduction of bacterial load, still some way from the positive control Tigecycline, which reduced the bacterial load by 3 logs.

Taken together, our results indicate that FITC-P33 reduce bacterial infections in vivo in different mouse models, but the molecule clearly needs further development to be suitable for therapeutic applications.

Discussion

The escalating threat of drug-resistant bacteria poses a critical challenge to global health, demanding innovative approaches in the development of antibacterial agents. The bacterial ribosome, the central hub of protein synthesis, has emerged as a promising target for antibiotic development[41]. There is a host of ribosome-targeting antibiotics and their mode of action spans many aspects of bacterial ribosome function and the corresponding sites on this macromolecular machine[41], although they all generally inhibit translational efficiency, i.e. lowering protein biogenesis or fidelity, i.e. introducing translational errors. In this study, we investigated a novel approach that targets bacterial protein homeostasis by inducing protein aggregation. Our findings indicate that the aggregation-prone peptide P33, whose APR was taken from the transmembrane region of an integral membrane proteins disrupts co-translational protein folding, affecting many proteins, but with a clear bias towards outer membrane proteins and finally leading to a collapse of proteostasis. The efficacy of P33 extends across a spectrum of gram-negative pathogenic bacteria, including drug-resistant strains of *A. baumannii, P. aeruginosa, K. pneumoniae, E. cloacae*, and *S. typhimurium*, and appears to work both during planktonic growth and in biofilm.

The P33 peptide is designed based on aggregation-prone regions (APRs) found in bacterial proteins, particularly those involved in transmembrane transport. This design strategy leverages the diversity of APRs present in the bacterial proteome, minimizing the risk of single resistance-conferring mutations. To elucidate the mode of action of P33, the study employed a range of techniques, including super-resolution structured illumination microscopy (SIM), scanning electron microscopy (SEM), fluorescent activated cell-sorting (FACS), proteomics, RNA sequencing, and CRIPSR-based genome engineering. The evidence supports the hypothesis that P33 initiates intracellular aggregation, as is seen from staining with amyloid-specific dyes and infrared absorbance spectra. In addition, several lines of evidence point to a co-translational mechanism of action: first, we showed that the inclusion bodies contain many ribosomal proteins and RNAs, but also mRNA species which notably correspond to the proteins found aggregated in the IBs. Second, when we inhibit translation using erythromycin, the induction of aggregation by P33 and downstream cell death is prevented. Third, ssrA-SmpB are recruited to the inclusion bodies and when we use CRISPR to change the ssrA-tag sequence to HA, we observe HA-tagging of nascent chains in response to P33 treatment. Since P33 did not act as a general ribosome inhibitor during in vitro translation experiments, we concluded that the molecule primarily targets nascent

https://doi.org/10.1038/s41467-025-56873-z

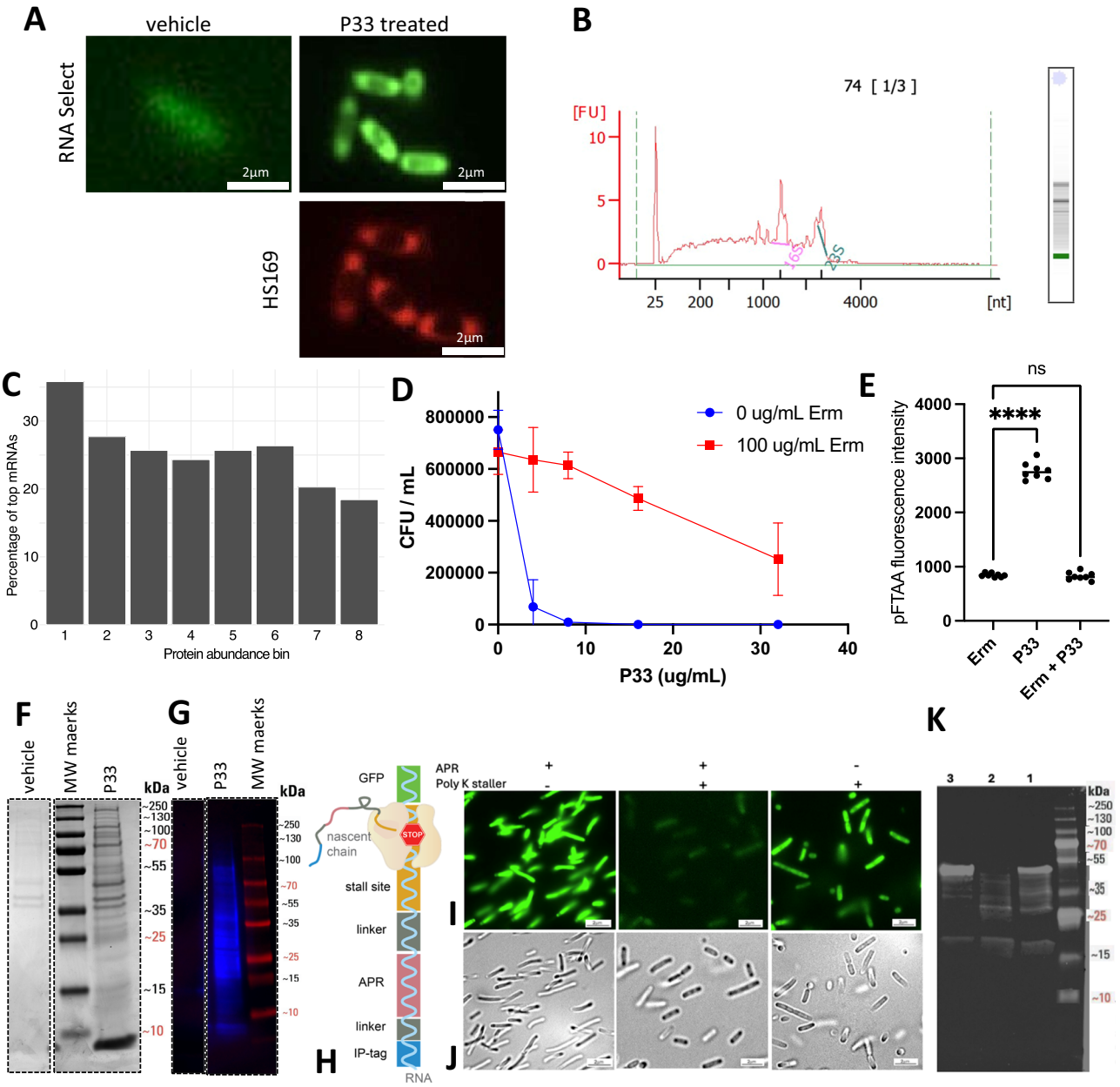

Fig. 5 | P33 treatment results in stalled ribosomes in inclusion bodies. A SYTO RNASelect nucleic acid staining of the *E. coli* bacteria treated by P33 or vehicle in (green) and HS169 staining (Red) to detect protein aggregation. The experiment was independently repeated three times with similar results. **B** Electropherogram profiles of RNA extracted from inclusion bodies, analyzed by capillary electrophoresis (Agilent 2100 Bioanalyser, RNA 6000 Pico Assay kit). Representative electropherograms are shown with peaks corresponding to 16S and 23S rRNA indicated. The experiment was independently performed three times, consistently yielding similar results. The RNA 6000 Pico Ladder well exhibits one marker peak (25 nt) and six distinct RNA peaks. **C** Bar plot showing the proportion of highly expressed mRNAs (top 500) across protein abundance bins (each with $n = 148$), sorted from most abundant (Bin 1) to least abundant (Bin 8). Higher abundance bins contain a larger proportion of highly expressed mRNAs, indicating a positive correlation between protein and mRNA levels. **D** pFTAA fluorescence intensity of the bacteria treated with P33 at MIC concentration, with or without erythromycin, to monitor aggregation. The data are presented as the mean fluorescence intensity with standard deviation (SD) from three independent biological replicates. Error bars represent the SD of the mean fluorescence intensity across these replicates. **E** Growth inhibition of *E.coli* cells treated with P33, with or without erythromycin (Erm, 100 µg/mL), Data represent the average and standard deviation of three replicates. Statistical analysis was performed using Brown-Forsythe and Welch ANOVA, followed by Dunnett's T3 test. Statistical significance is indicated as follows: */ = $p < 0.05$, **$p < 0.01$, ***/ = $p < 0.001$ and ****/ = $p < 0.0001$. SDS-PAGE with Coomassie staining (**F**) and Western blot (**G**) analysis of the HA-tagged species in the IB fraction from bacteria treated with P33 or vehicle at MIC concentration. The experiments were conducted at least three times, **(H)** Diagram of an artificial construct with a ribosome stalled with a nascent chain exposing an APR. A C-terminal GFP tag is included to detect full-length constructs. There are 3 constructs: The APR disrupted through mutation (SVIDDSLGN) and a ribosome polylysine stalling site, the intact APR (SVIIWSLGN) with the stalling sequence (Line 2), and the construct with the intact APR but no stalling sequence. **(I)** SIM images of *E. coli* BL21 bacteria harboring the same constructs from H. The experiments were performed at least three times **(J)** Phase contrast images of the *E. coli* BL21 bacteria containing the same construct plasmid from H showing the inclusion bodies in the bacteria. **K** Western blot analysis of GFP-tagged proteins from H, I, J. Proteins were separated by SDS-PAGE, transferred to a nitrocellulose membrane, and probed with an anti-GFP antibody for detection. Molecular weight markers are shown on the right. The experiments were performed three times.

https://doi.org/10.1038/s41467-025-56873-z

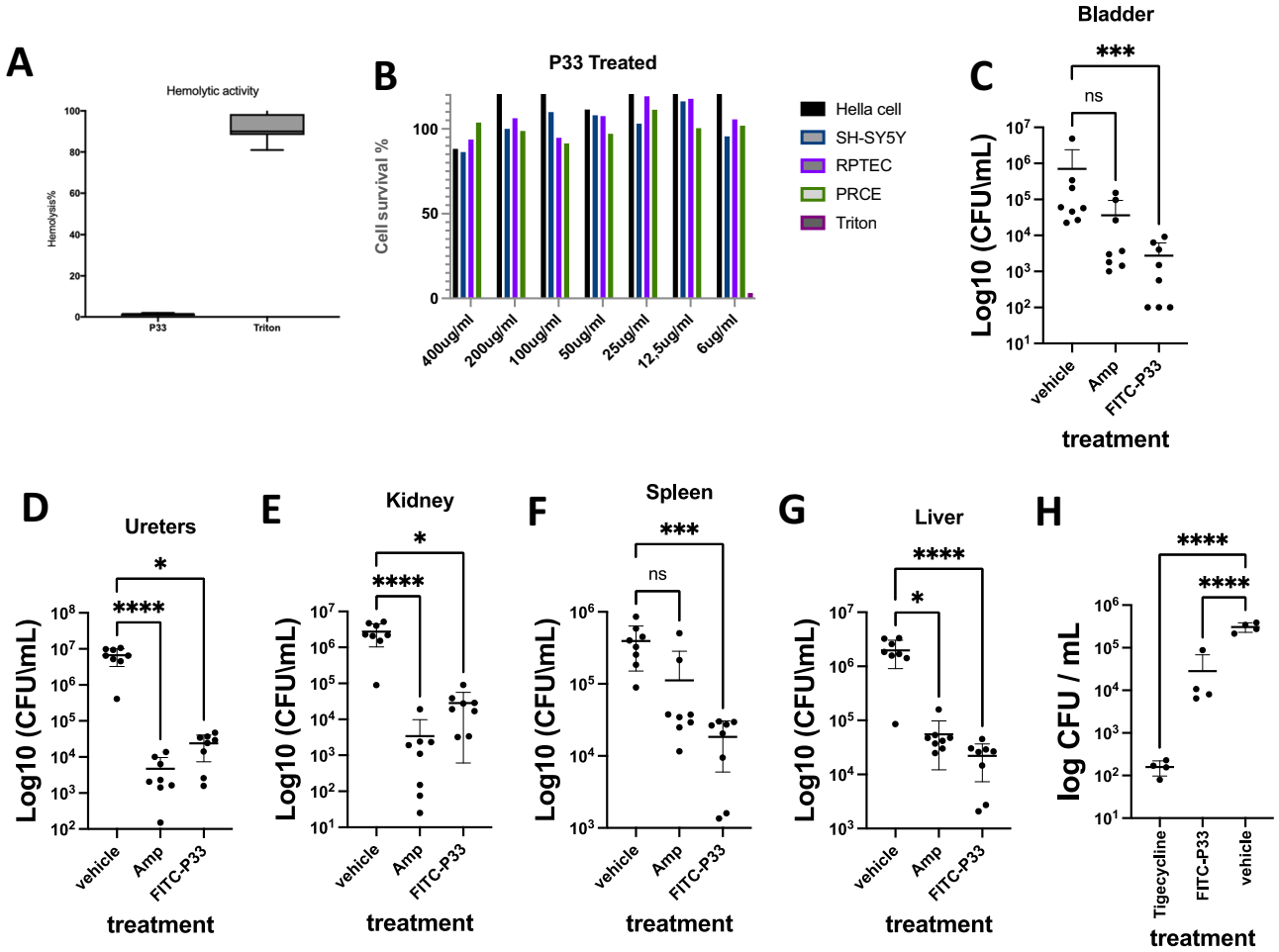

Fig. 6 | Evaluation of P33 efficacy in vivo. A Hemolysis of human erythrocytes was assessed in the presence of P33 peptides for 2 hours at 37 °C and normalized to the value obtained with 1% Triton X-100. The plot shows mean values ± standard deviation (SD) from three replicates. For the box plot, the center line represents the median, the bounds of the box indicate the interquartile range (IQR), and the whiskers represent the minima and maxima within 1.5 times the IQR. **B** Cell viability, measured using the CellTiter Blue assay, of various mammalian cells (Hela, SH-SY5Y, RPTEC, and PRCE cells) treated for 24 hours with the indicated concentrations P33 at 37 °C. The plot represents the mean and standard deviation from three replicates. Antibacterial efficacy of FITC-P33 in a mouse model of bladder infection with *E. coli*. The bacterial load of mice infected with *E. coli* transurethral was determined after treatment with FITC-P33 (IV, 10 mg/Kg) or Ampicillin as a positive control (Oral, 30 mg/Kg) and vehicle treatment as negative control (IV) in (**C**) bladder, (**D**) ureter, (**E**) kidney, (**F**) spleen and (**G**) liver. Each group consisted of 8 animals, and bacterial loads are expressed as log10 (CFU/mL). **H** Antibacterial efficacy of P33 in a mouse sepsis model of *Acinetobacter baumannii* ATCC 19606. Animals were infected interperitoneally, and 1 hour and 3 hours post infection the animals were treated with FITC-P33 (10 mg/Kg subcutaneously), Tigecycline (30 mg/Kg subcutaneously) and vehicle were used as positive and negative control, respectively. Blood samples were collected 24 hours post-infection, and bacterial CFU counts per mL of blood were determined. Data are presented as mean values ± standard deviation (SD). The *p*-values were calculated using a one-way ANOVA. Statistical significance is indicated as follows: */ = $p < 0.05$, **= $p < 0.01$, ***/ = $p < 0.001$ and ****/ = $p < 0.0001$.

chains during translation. However, further unraveling the exact intricacies of the MoA, beyond the observation that the scale of aggregation involves the entire ribosome plus many transcripts and nascent chains, remains challenging, and several questions still persist.

One of which concerns the specificity of the initial peptide interactions. Our proteomic analyses identified nascent chains with homologous APRs immediately upon P33 treatment, which would be consistent with our design principles. However, we also observed the accumulation within IBs of many proteins that lack such homologous regions, suggesting several potential scenarios for P33's broad-spectrum activity: (1) Initial engagement with nascent chains with homologous APRs, such as OmpA, leads to a rapid disruption of protein homeostasis, resulting in widespread aggregation, possibly through the sequestration of molecular chaperones and other quality control components. (2) The initial engagement with the nascent chains is based on general parameters, such as hydrophobicity and charge, lacking sequence-specific interactions, which leads to the same rapid loss of proteostasis. While this mechanism could imply off-target effects in mammalian cells, the lack of observed toxicity in mammalian models might be explained by differential uptake between bacterial and host cells. (3) Our data do not fully exclude the possibility of a direct interaction with an element of the ribosome or ribosome-rescue pathway, which could lead to a loss of ribosomal quality control and, eventually, a loss of proteostasis. Although the in vitro translation assays argue against this scenario, it has been shown that ribosomes are prone to co-aggregation when confronted with aggregating proteins[42]. The authors of that study proposed that this may be facilitated by charge interactions between the negatively charged ribosomal RNA and the positively charged protein they were studying (lysozyme)[42]. However, despite our P33 peptide being highly charged, the interaction does not take place in the presence of erythromycin, a ribosome inhibitor, suggesting that this is not the mode of action of our peptide. Regardless of the trigger of the aggregation process, it has been shown that ribosomal proteins are themselves aggregation-prone and orphan ribosomal proteins are proteotoxic and impair cellular function[43]. This suggests that these factors may contribute to the antibacterial effect of P33.

In conclusion, this study opens new avenues for the development of antibacterial therapeutics by disrupting membrane protein homeostasis. The unique mode of action exhibited by P33, its broad-spectrum activity, and its promising in vivo efficacy highlight the potential of this strategy in addressing the urgent challenge of drug-resistant bacterial infections. Further research and optimization efforts will be essential to translate these findings into clinically relevant antibacterial agents.

Methods

Bioinformatics analysis

Protein sequences of bacterial strains were obtained from UniProt[44]. We employed the software algorithm TANGO[45] to identify APRs across this work, using a score of 5 per residue as the lower threshold and a parameter configuration of temperature at 298 K, pH at 7.5, and ionic strength at 0.05 M. Gene ontology enrichment analysis was done using the clusterProfiler v4.12.6 package in R[46]. Isoelectric points and net charge of bacterial proteins were calculated using the Peptides v2.4.6 package in R[47]. Secondary structured propensity was calculated using DSSP[48,49] from the xssp-3.0.10 software on the corresponding AlphaFold protein structures[50,51].

Peptides design, synthesis and purification

Peptides were ordered from Genscript at >90% purity and were also produced in-house using the Intavis Multipep RSi automated synthesizer using solid-phase peptide synthesis. After synthesis, crude peptides were stored as dry ether precipitates at −20 °C. Stock solutions of each peptide were either prepared in 100% DMSO (only for initial screening assays) or following the optimized protocol: peptides were dissolved in 1 M NH4OH, allowed to dissolve for ~5 minutes, and dried in 1.0 ml glass vials with an N_2 stream to form a peptide film. This film was dissolved in a buffer containing 50 mM Tris (pH 8.0) and 20 mM guanidine thiocyanate. Peptides were N-terminally acetylated and C-terminally amidated.

Bacterial strains and growth conditions

Reference bacterial strains were purchased from ATCC: *Escherichia coli* (ATCC 25922, LMG 8223), *Klebsiella pneumoniae* (ATCC 13883, LMG 2095), *Enterobacter cloacae* (ATCC 13047, LMG 2783), *Acinetobacter baumanni* (ATCC 19606, LMG 1041), *Pseudomonas aeruginosa* (ATCC 27853, LMG 6395), *Staphylococcus aureus* (ATCC 25213, LMG 10147). Multidrug-resistant bacterial species, including *E. coli, A. baumannii, P. aeruginosa, K. pneumoniae, E. cloacae, S. typhimurium, S. aureus MRSA* and *S. epidermidis* were sourced from UZ Leuven University hospital. Species identification and antibiograms for all clinical isolates conducted using MALDI-TOF mass spectrometer and VITEK® 2 automated system (bioMérieux). Colonies were grown on a Mueller Hinton (MH) agar plate at 37 °C overnight. The colonies were used to inoculate 5 mL fresh MHB media and grown at 37 °C.

Construction of the *ssrA*-HA tag reporter strain

To insert the HA tag into the *ssrA* gene, we used the BW25113-derived deletion mutant JW2601 from the Keio collection, in which *smpB* is replaced with a kanamycin resistance cassette.[52]. In this *E. coli* background, the CRISPR[53] plasmids, pCas9 and pKDsgRNA-FRT were sequentially transformed[54] and plated on LB agar medium contaning 30 μg/mL chloramphenicol and 50 μg/mL spectinomycin. The rescue oligo, including the HA tag-integrated *ssrA* sequence, the native *smpB* gene, and the up-and downstream homologous tails, was prepared using splicing by overlap extension (SOE) PCR. To this end, the region upstream of the HA tag-insertion site was amplified with Q5 polymerase (New England Biolabs) and primers, gccttagagacatctaccgcc and TCTGGAACATCGTATGGGTAAGATCcgactatttttgcggcttttac, whereas the downstream fragment was created using primers ACCCATACGATGTTCCAGATTACgcttaataacctgcttagagccctc and ataaagctggtaatcggcatc. The resulting PCR products were purified using Mag-Bind® TotalPure NGS beads (Omega Bio-tek) and mixed in equimolar quantities (10 nM) in a 10-cycle PCR reaction (annealing temperature: 59 °C) without any primers. Thereafter, the desired SOE product was enriched (in 25 cycli, annealing temperature: 61 °C) using the previously specified gccttagagacatctaccgcc, and ataaagctggtaatcggcatc primers and extracted from a 0.7 (w/v) % agarose gel using the Wizard® SV Gel and PCR Clean-Up System (Promega). The purified *ssrA*-HA tag reporter construct was integrated into the JW2601 genome according to the CRISPR protocol as described by Swings et al. (2018)[54]. After completing CRISPR, the region surrounding the *ssrA*-HA locus was amplified using the ggcgtaaacttccatccacc and tcgctgcttggtcaaagg primers and this PCR product was sent for Sanger sequencing (Macrogen Europe). Finally, the CRISPR plasmids were cured from the successful clone following the procedure of Reisch and Prather (2015)[55].

Minimal inhibitory and bactericidal concentration assays

The MIC was determined as the lowest peptide-concentration that completely inhibited visible bacterial growth as assessed using a broth microdilution assay in accordance with EUCAST guidelines. The assay was conducted in a 96-well polystyrene flat-bottom microtiter plate (BD Biosciences). Briefly, a single bacterial colony was inoculated in MH broth medium and incubated at 37 °C overnight. Several colonies of the fresh cultures were diluted to 10^6 cells/ml in fresh MH broth medium. Peptides were dissolved in freshly prepared 6 M urea before use. In each well of the sterile 96-well plate, 50 μL of MH broth medium with different concentrations of peptides ranging from 120 to 2 μg/mL were prepared. Afterwards, 50 μL of the diluted bacteria were pipetted into each well. For controls, the growth of bacteria in the presence of the maximum concentration of carrier was considered the positive control, and growth in the medium alone was considered the negative control. The plates were incubated overnight at 37 °C to allow bacterial growth. Bacterial growth was measured by the OD at 590 nm using a Perkin Elmer spectrophotometer (1420 Multilabel Counter Victor 3). The MBC test defines the lowest concentration of the peptide that kills 99% of bacteria which was determined via CFU counting method.

Antibody and antibiotic product codes

GFP Antibody (Polyclonal Rabbit antibody, Cell Signaling Technology, catalog number 2555S, clone: Polyclonal. This antibody detects GFP-tagged proteins. It was used at a dilution of 1:1000. Store at −20 °C.

Anti-HA Tag Rabbit Polyclonal Antibody (Covance, catalog number PRB-101P, clone: HA.11. This antibody recognizes the hemagglutinin (HA) epitope tag sequence YPYDVPDYA. It was used at a dilution of 1:1000. Store at −20 °C.

Rabbit Anti-Mouse IgG HRP (Abcam, catalog number ab6728. This antibody was conjugated to Horseradish Peroxidase (HRP) for detection in Western Blotting. It was used at a dilution of 1:5000. Store at −20 °C.

Goat Anti-Chicken HRP (Abcam, catalog number ab97135. This antibody was conjugated to Horseradish Peroxidase (HRP) for detection in Western Blotting. It was used at a dilution of 1:5000. Store at −20 °C.

The antibiotics used for this study: Ampicillin (Duchefa Biochemie, Netherlands, A0104.0025), Colistin sulfate salt (CAS Number: 1264-72-8), Tigecycline (Sigma-Aldrich, Y0001961), erythromycin, CAS number 114-07-8 (Sigma-Aldrich, catalog # E5389), and kanamycin CAS number 56-75-7 (Duchefa Biochemie).

Measurement of hemolytic Activity

The hemolytic activity of peptides was determined by measuring hemolysis of human erythrocytes (RBC). Pooled fresh blood was obtained from healthy volunteers (Red Cross Flanders) and erythrocytes were collected by centrifugation 1000 × *g* for 5 minutes

(anticoagulated by EDTA). The pellet was washed three times with phosphate-buffered saline (PBS) before use and diluted to a concentration of 8% in PBS. 100 µL of 8% red blood cells solution was mixed with 100 µL of serially diluted peptides in PBS buffer in 96- well plates (BD Biosciences). The mixtures were incubated for 1 hour at 37 °C. Thereafter, the plate was centrifuged for 10 min at 1000 × *g* and 100 µL of supernatant was transferred to a sterile 96-well plate (BD Biosciences, flat bottom). The release of hemoglobin was determined by measuring the absorbance of the supernatant at 405 nm. The hemolytic activity was determined as the minimal peptide concentration that caused hemolysis (minimal hemolytic concentration). Erythrocytes in 1% Triton and maximum used concentration of vehicle were used as controls of 100 and 0% hemolysis, respectively.

Cell toxicity assay

Cell Titer Blue (Promega) method was used to measure the cytotoxicity of P33. Briefly, HeLa cells (obtained from the European Collection of Authenticated Cell Cultures (ECACC), catalog number 93021013), SH-SY5Y cells (obtained from the American Type Culture Collection (ATCC), catalog number CRL-2266), Primary Renal Proximal Tubule Epithelial Cells (RPTEC) (normal human, obtained from ATCC, catalog number PCS-400-010™), and Primary Renal Cortical Epithelial Cells (HRCE) (normal human, obtained from ATCC, catalog number PCS-400-011) were seeded in 96-well round-bottom plates at a density of 3 × 105 cells/ml in Dulbecco's modified Eagle's medium and treated with different concentrations of peptides. Cells treated with 1% Triton X-100 and vehicle were considered as positive and negative controls, respectively. Microplates were incubated at 37 °C with 5% CO_2 and 90% humidity for 4 hours. The micro-plate was centrifuged at 200 × *g* for 10 minutes. One hundred microliters of supernatant were transferred to a clean 96-well flat-bottom microplate. Cell viability was calculated using the formula: (exp.value − negative control value)/ (positive control value − negative control value) ×100 after measuring the absorbance of the samples at 490 nm. The amount of absorbance is proportional to the number of living cells and corresponds to their metabolic activity. Cell lines were regularly tested for mycoplasma contamination.

Flow cytometry analysis

Flow cytometry was employed to evaluate peptide uptake and its correlation with bacterial death. Briefly, at end-exponential growth phase, bacteria were washed two times with PBS (8000 rpm, 4 minuts), thereafter they were diluted to McF 0.5 (10^7 CFU mL^{-1}) in sterilized PBS. 500 µL bacteria (solution/ sample) was treated with carboxyfluorescein-labeled peptide at the MIC concentration or HS169 (50 uM) at the appropriate time of incubation. Treated bacteria were washed three times with PBS. 1 µL of propidium iodide (PI) was added to 500 µL bacteria and incubated for 10 minutes. All samples were acquired on a GalliosTM Flow Cytometry and analyzed with Flowjo software version 10.6.

Visualization of the inclusion bodies using structured illumination microscopy

To verify protein aggregation in the bacteria (different species of bacteria were used for this study) upon peptide treatment, 1 mL of 10^6 CFU bacteria were first treated with peptides at the corresponding MIC concentration, and with colistin at an MIC of 1 µg/mL. Following treatment, the bacteria were stained with 50 µM pFTAA and incubated at 37 °C for at least 40 minutes. Subsequently, the bacteria were centrifuged at 8000 rpm for 5 minutes, and the pellet was resuspended and pipetted onto slides for imaging with Structured Illumination Microscopy (ZEISS Zen 2010D software). Vehicle-treated bacteria served as a negative control. Image analysis was performed using the FIJI (ImageJ 2.3.0) software.

In Vitro Expression of mGreenlantern Using PURExpress

mGreenlantern was expressed using the PURExpress® in vitro transcription-translation system (New England Biolabs) according to the manufacturer's instructions. The template for the transcription/ translation reaction was generated via PCR with primers designed to overlap the gene of interest, incorporating a T7 promoter and a T7 terminator sequence. Template DNA was purified using Qiagen MinElute PCR purification columns. P33 was prepared at a stock concentration of 2 mg/ml in DMSO and subsequently diluted 1:10 in physiological water to achieve a 200 µg/ml solution. This solution was further diluted for the reactions, with a 0.5% DMSO solution added to equalize DMSO concentrations across samples (final concentration: 0.08% DMSO). A total of 250 ng of template DNA was added to each in vitro translation reaction, which proceeded at 37 °C for 2 hours with double orbital shaking at 500 rpm. GFP fluorescence was measured using a CLARIOstar plate reader (BMG Labtech), utilizing an excitation filter of 470-15 nm and an emission filter of 515-20 nm.

Primers Used

- **Forward Primer:** GCGAATTAATACGACTCACTATAGGGCTTAAGTATAAGGAGGAAAAAATATGTGGAGCCATCCGCAGTTTGAAAAA
- **Reverse Primer:** AAACCCCTCCGTTTAGAGAGGGGTTATGCTAGTTAtttatacagttcgtccatatcgtg

In vivo animal experiments

All animal experiments were conducted in a blinded manner. Female C57BL/6Jax mice, aged 5 to 8 weeks and weighing between 18 and 22 grams, were used in this study (KU Leuven). Mice were housed in plastic cages with five mice per cage, using softwood granules as bedding. The housing environment was maintained at a temperature between 21 °C and 25 °C with a 12-hour light-dark cycle. The animals had unrestricted access to water and pelleted rodent food. In minimize stress-induced confounding factors, the mice were acclimated to the laboratory environment for one week prior to experimental procedures. All animal experiments were conducted in compliance with international animal welfare standards and were approved by the local Animal Ethics Committee. The specific ethical approvals and protocol numbers for each experiment are provided in the relevant sections of the manuscript.

Dose escalation study of the peptide in vivo

The procedures were approved by the local Animal Ethics Committee and comply with international animal welfare standards (Approval P067/2015 from the Ethical Committee of KULeuven). Male C57BL/6 mice, aged 5 to 8 weeks, were used for this study. The dose escalation study was conducted with limited number of mice (n = 4 per dose level) and a involved administering only one dose level per animal. The doses included 3, 5, 10, 15, and 30 mg/kg were considered for this experiment. The FITC-labeled peptides were administrated via intravenous (IV), intraperitoneal (IP), or subcutaneous (SC) routes. Mice were closely monitored for any adverse effects throughout the study.

Urinary tract infection model

The urinary tract infection model was conducted as described previously[12,14]. The urinary tract infection model was conducted as previously described12,14. Female C57BL/6 Jax mice (substrain: C57BL/6 J), aged 5 to 8 weeks and weighing between 18 and 22 grams, were used for this study (Approval P034/2019 by the Ethical Committee of KULeuven). Groups of 8 animals per treatment group were included in the study. Female mice were chosen for this model due to their shorter urethra, which is more susceptible to urinary tract infections. Briefly, mice were anaesthetized via intraperitoneal administration of ketamine/ xylazine. The bladder was then palpated to expel any remaining urine. Using a sterile catheter, anaesthetized mice were inoculated with 50 µL of bacterial suspension (1E10^8 CFU/mL) in the bladder over 5 seconds.

One- or five-hours post-infection, mice were randomized and treated in three groups of P33 peptide (IV, 10 mg/kg), vehicle and ampicillin (orally, 30 mg/kg) treatment. After surgery, the animals were visually monitored for a full recovery. Twenty-four hours post-infection, mice were sacrificed, and corresponding organs (kidney, bladder, ureter) were washed with PBS and homogenized for 24 seconds (Thermo Savant FastPrep FP120 Homogenizer). The homogenized tissues were serially diluted and cultured on MH plates. The plates were incubated overnight at 37 °C and CFUs were counted.

Septicemia murine infection model induced by *Acinetobacter baumanni* ATCC 19606

Male C57BL/6 mice (substrain: C57BL/6J), aged 5–8 weeks and weighing 18–22 grams, were used in this model (Approval P091/2019 by the Ethical Committee of KU Leuven). The study included 4 animals in each treatment group. A safe concentration of peptides of 30 mg/kg was used for this experiment. A peptide concentration of 30 mg/kg, determined to be safe based on prior escalation studies, was used. This dose, administered intraperitoneally, did not result in any acute adverse effects. Mice were infected with A. *baumanni* ATCC 19606 (10^6 CFU/mouse in 5% NaCl-mucin) via intraperitoneal delivery. Following infection, mice were treated either with the corresponding vehicle (saline, administered subcutaneously), peptide P33 (10 mg/kg subcutaneously), or tigecycline (30 mg/kg subcutaneously) as a positive control, at 1- and 3-hour post-infection. Blood was collected via retro-orbital puncture into heparinized tubes for bacterial quantification. Immediately after collection, blood was serially diluted, plated on Tryptic Soy Agar (TSA), and incubated overnight at 37 °C in ambient air. Bacterial colonies were counted to determine the bacterial burden (CFU) for each dilution, and the bacterial burden was calculated for each mouse.

Scanning electron microscopy

Bacterial cells in end-exponential growth phase were washed with PBS and then diluted to a density of 10^8 CFU/mL. They were treated with peptides at appropriate concentrations, depending on the bacterial species, or Colistin for *E. coli* at MIC concentration of 1 µg/mL. After a 2 h treatment, bacterial cells were collected using nitrocellulose membrane filters (0.1 µm CAS 900470.0 Ref. VCWP0/300) and subsequently fixed with 2% glutaraldehyde for 1 h. The samples were then post-fixed with 1% osmium tetroxide (OsO4) in 0.1 M sodium cacodylate buffer for 1 h. Samples were washed three times with cacodylate buffer (0.1 M sodium cacodylate) for 10 minutes at room temperature (RT). The samples were dehydrated with a graded ethanol series (50, 70, 96, and 100% alcohol). After the dehydration step, samples were dried by hexamethyldisilazane for 1 hour and mounted on the specimen stubs and sputter coated with gold. A SEM-FEG (field emission guns) microscope (JEOL JSM 6700 F) with an accelerating voltage of 30 kV was used.

Cross-Section TEM

Escherichia coli at the end-exponential growth phase were washed, diluted in physiological water, and treated at 37 °C for 1 hour with either the MIC of specific aggregator peptides or buffer (Control group). Cells were then centrifuged at 4,000 × g for 4 minutes, and the resulting pellets were fixed in 2.5% glutaraldehyde in 0.1 M Na-cacodylate buffer (pH 7.2–7.4) with 2.5 mM $CaCl_2$ and 1 mM $MgCl_2$ for 1 hour.

Following fixation, pellets were washed with cacodylate buffer, resuspended in 1.5% low melting point agarose (40 °C), and centrifuged again. The chilled pellets were sectioned into 1 mm^3 cubes, post-fixed with 1% OsO_4 in distilled water for 2 hours, and washed twice. The samples were then dehydrated in a graded ethanol series (30%, 50%, 70%, 90%, 100% for 10 minutes each, repeated three times), treated with propylene oxide, and infiltrated with a 1:1 mixture of epoxy resin and propylene oxide. After overnight infiltration, the samples were transferred to fresh epoxy resin, embedded in BEEM capsules, and polymerized at 60 °C for 2 days.

Ultrathin sections were prepared using a Leica Ultracut UCT ultramicrotome and observed with a JEOL JEM-1400 TEM at 80 kV, equipped with an Olympus Quemesa 11 Mpxl camera.

Atomic Force Microscopy-based Infrared Spectroscopy (AFM-IR)

E. coli (ATCC 25922) were treated with 6 µg/mL P33 for 60 minutes, fixed and dried following the SEM preparation. Then they were spun down and resuspended in a graded series from propylene oxide to Agar 100 epoxy resin. The resin was cured at 60 °C for two days. Sections of 100 nm thick were made with a Leica Ultracut ultramicrotome, deposited on a silicon wafer, and imaged in a nanoIR3 (Bruker, Germany). A field of view of 20 × 20 µm and 512 × 512 pixels was imaged at 0.1 Hz line rate, AFM I gain 1, AFM P gain 2, wavenumber 1650 cm^{-1}, laser power 1.37%, PLL I gain 3 and PLL P gain 30, with pulse frequency approximately 700 kHz. Spectra were collected with PLL I gain of 0.1 and P gain of 1. They were normalized to the beam power spectrum, divided by the average epoxy spectrum, and min-max normalized, using Python 3.10.12 with packages anasys-python-tools (0.4.1), scipy (1.12.0), scikit-image (0.19.3), xarray (2023.7.0), matplotlib (3.8.3) and seaborn (0.13.2).

Macrolide and peptide interaction method

To evaluate the effect of peptides in the presence of erythromycin, bacteria were grown in 5 mL of LB medium. Exponential-phase cultures were then diluted to 10^8 cells/mL. The bacterial cells were treated with erythromycin at the concentration of 100 µg/mL for 3 hours at 37 °C without shaking to halt their growth. Different concentrations of peptides (ranging120 to 2 µg/mL) or buffer were dispensed into 96-well plates, with at least three replicate wells per conditions (50 µL per well). 50 µL of erythromycin-treated bacteria were added to each well and the plate were incubated for 2 hours at 37 °C. After this incubation period, the bacterial cells were serially diluted and plated on blood agar plates. The blood agar plates were then incubated overnight at 37 °C. The number of viable cells was determined by counting colony-forming units (CFUs).

IB purification

Bacterial cultures were centrifuged for 30 minutes at 4000 × g and cells were washed with physiological water (0.9% NaCl). The bacterial cells were then treated with peptides at the appropriate concentrations for at least 2 hours at 37 C. The bacterial pellets were washed with 10 mL buffer A (50 mM HEPES, pH 7.5, 300 mM NaCl, 5 mM β-mercaptothions, 1.0 mM EDTA) and centrifuged at 4 °C for 30 minutes at 4000 × *g*. The supernatant was discarded and 20 mL of buffer B (buffer A plus 1 tablet of the protease and phosphatase Inhibitor Cocktail (ab201119, Abcam, UK)) was added to the bacterial pellet. To lyse the cells, a High-Pressure Homogenizer (Glen Creston Ltd) set to 20,000–25,000 psi was used on ice. In addition, the suspensions were sonicated on ice using a Branson Digital Sonifier (50/60 Hz). Sonication was performed in alternating 2-minute cycles (15 pulses of 5 seconds at 50% power with 30-second pauses on ice), until a total of 2 minutes of sonication was achieved. The lysed cells were then centrifuged at 4 °C for 30 minutes at 11,000 × *g*.

The resulting pellet was resuspended with 10 mL buffer C (buffer A plus 0.8% (V/V) Triton X-100, 0.1% sodium deoxycholate), and sonicated to ensure the complete dissolution of the pellet. This step was repeated three times. Centrifugation was then performed at 4 °C for 30 minutes at 11,000 × *g*. Finally, to solubilize IBs, the pellet was resuspended in 500 µL of buffer D (50 mM HEPES, pH 7.5, 8.0 M urea).

Time-Resolved Mass Spectrometry and data analysis of P33-Treated Bacterial IBs

In this experiment, bacteria were exposed to P33 at its Minimum Inhibitory Concentration (MIC) for various durations: 0, 5, 10, 20, 40, and 60 minutes. After each interval, the bacterial cells were fixed with 4% paraformaldehyde to preserve their structure. We then separated the soluble and inclusion body (IB) fractions for protein analysis using gel-free mass spectrometry. This approach allowed us to identify and quantify proteins, providing insights into the changes induced by P33 over time.

For mass spectrometry analysis, dithiothreitol (DTT) was added to reduce disulfide bonds in the soluble and IB fractions, followed by iodoacetamide (IAA) to alkylate cysteines and prevent bond reformation. Ammonium bicarbonate (ABC) was then added, and samples were digested with trypsin at 37 °C for at least 16 hours. The resulting peptides were purified using C18 spin columns to remove contaminants and were resuspended in 5% acetonitrile (ACN) and 0.1% formic acid (FA) for injection into the Q Exactive Orbitrap mass spectrometer.

The high-resolution mass spectrometry data were analyzed to capture detailed protein information across different time points, providing a comprehensive view of P33's impact on the bacterial proteome.

After digestion, 5 μL of each sample was separated using an Ultimate 3000 UPLC system with a C18 column under a linear gradient of acetonitrile and formic acid. The peptides were introduced into the Q Exactive Orbitrap mass spectrometer, operated in positive ion mode with a nano spray voltage of 1.5 kV and a source temperature of 250 °C. Calibration was performed with a ProteoMass LTQ/FT-Hybrid mix and lock mass, and data acquisition was conducted in data-dependent mode. Precursor ions were scanned at a resolution of 70,000 (m/z 400–1600), followed by MS/MS scans for the top 10 most intense ions. The resulting spectra were analyzed using MASCOT software server 2.8 against the UniProt *E. coli* database, with parameters set for precise tolerance and modification identification. The identification of differentially expressed proteins between the soluble and IB fraction was done using the limma R package[56].

RNA purification from inclusion bodies

Twenty milliliters of bacterial culture in the exponential growth phase were centrifuged for 30 minutes at 4000 × *g* and washed with physiological water. The bacterial pellets were washed with 10 mL buffer A (50 mM HEPES, pH 7.5, 300 mM NaCl, 5 mM β-mercaptothion, 0.1 mM EDTA) and centrifuged at 4 °C for 30 minutes at 4000 × *g*. The supernatant was discarded and 20 mL of buffer B (buffer A plus two tablets of proteinase inhibitor cocktail) was added to the bacterial pellet. To break the cells, a Glen Creston Cell Homogenizer with pressure set to 20,000–25,000 psi was used three times in the cold room. The lysed cells were centrifuged at 4 °C for 30 minutes at 11,000 × *g*. The precipitated fraction was afterwards re-suspended with 5 mL buffer D (buffer A plus: 0.8% (V/V) Triton X-100, 0.1% sodium deoxycholate) and mixed carefully to ensure the pellet is completely dissolved. This step was repeated three times. Centrifugation was performed at 4 °C for 30 minutes at 11,000 × *g*. The pellet was then used for the RNA extraction using RNA mini kit Bio-Rad (Aurum Total RNA Mini Kit) by adding lysozyme and proteinase K to disrupt the aggregated protein and the process continued according to the standard protocol provided by Bio-Rad.

Quartz Crystal Microbalance with Dissipation monitoring Methods

For all experimental preparations, filtered and UV-treated ultrapure water with a resistivity of 18.2 MΩ.cm was used (Sartorius AG, Gottingen, Germany). The reagents used in preparation of various HEPES buffers were HEPES (≥99.5%, Sigma Aldrich, St. Louis, USA), NaCl, potassium chloride (KCl, Sigma Aldrich, St. Louis, USA), and calcium chloride ($CaCl_2$, anhydrous, Sigma Aldrich, St. Louis, USA). Buffers were passed through a hydrophobic polypropylene membrane filter (GH Polypro, 0.2 μm, PALL Life Sciences, USA) before use and stored at 4 °C. 1-Palmitoyl-2-oleoyl-sn-glycero-3-phosphocholine (POPC, >98%) and 1-palmitoyl-2-oleoyl-snglycero-3-phospho-(1'-rac-glycerol) (POPG, >98%) were obtained from Avanti Polar Lipids, Inc. (Alabaster, AL).

To form liposomes, the lipids were suspended in 1 mL of HEPES buffer (0.5 mM lipid, 10 mM HEPES, 150 mM NaCl, pH 7.4), incubated on ice for at least 30 min, vortexed for 5 min, and finally 15 times extruded through polycarbonate membranes (0.1 μm, Avanti Polar Lipids, Inc., Alabaster, AL). The liposomes were then diluted to 5 mL using another HEPES buffer (0.1 mM lipid, 10 mM HEPES, 150 mM NaCl, 5 mM $CaCl_2$, pH 7.4) The lipids were in liquid phase state under experimental conditions at 22 °C.

QCM measurements were performed using silicon dioxide (SiO_2)-coated sensors with a fundamental frequency of 5 MHz on a Q-Sense E4 instrument (Biolin Scientific, Gothenburg, Sweden). All measurements were conducted at 22 ± 0.05 °C To clean the sensors prior to each measurement, the sensors were soaked in 2% Hellmanex II solution (Hellma, Mülheim, Germany), then rinsed sequentially with ultrapure water and isopropanol (>99.5%, Merck, Germany) and dried under a gentle stream of N_2. The dry sensors were then treated with a UV ozone clean (BioForce Nanosciences, Virginia Beach, USA) for 20 minutes immediately prior to the start of the measurement.

To begin the measurement, an ultrapure water baseline was recorded for at least 30 minutes at a flow rate of 200 μL/min, followed by the lipid dilution buffer at 200 μL/min (10 mM HEPES, 150 mM NaCl, and 5 mM $CaCl_2$). Lipid liposomes flowed into the chamber at 50 μL/min until the liposomes ruptured occurred and a bilayer assembled on the sensor surface. Buffer was reintroduced at 200 μL/min to remove any excess lipid and to re-establish a baseline for the experiment.

Peptide solutions were created at the desired concentrations (1, 10, and 50 μM) in the lipid dilution buffer and introduced at 50 μL/min for 12 minutes. Changes in frequency and dissipation were measured for another 48 minutes without any flow. The flow cell was subjected to a buffer wash using the HEPES lipid dilution buffer at 200 μL/min for 15 minutes. Changes in frequency (Δf) were measured over time while the quartz crystal sensors were excited at multiple harmonics ($n = 1, 3, 5, 7, 9$, and 11; 5–55 MHz, respectively). Data for the 3rd, 5th, 7th, and 9th harmonics were used for analysis. QCM data were exported from QTools (Q-Sense, Biolin Scientific, Gothenburg, Sweden).

Biofilm formation assay

Biofilm formation of peptide-treated *E. coli* Keio and *S. aureus* was quantified using crystal violet staining, following a similar procedure as described previously[57]. Overnight cultures were diluted to an OD600 of 0.005, and a volume of 200 μL was added to the wells of a 96-well microtiter plate. The plate was then incubated at 37 °C for 24 hours. Following incubation, remaining planktonic bacteria were removed, and various concentrations of the peptides or vehicle were added to each well. The plate was incubated for 2 hours. After 2 hours the wells were rinsed three times with PBS and dried for 1 hour at room temperature. The dried biofilms were stained with 200 μL 1% (w/v) crystal violet (Sigma) for 10 minutes. This was followed by three washes with water and drying. The stained biofilms were released using 200 μL of 30% (v/v) acetic acid solution and quantified by measuring the absorbance of crystal violet at 585 nm in a UV/VIS plate reader. The biofilm formation of each culture was normalized relative to negative control samples. P-values were calculated using a two-tailed, equal variance t-test.

RNA sequencing

RNA quality control. RNA concentration and purity were determined spectrophotometrically using the Nanodrop ND-1000 (Nanodrop Technologies) and RNA integrity was assessed using the Bioanalyzer 2100 (Agilent).

Library preparation. For each sample, 100 ng of total RNA was used as input, using the Illumina Stranded Total RNA Prep, Ligation with Ribo-Zero Plus Kit (protocol version: #1000000124514 v02 (April 2021)). Initially, abundant rRNA molecules are first depleted from total RNA by means of DNA probes which bind to the rRNA molecules; both are then enzymatically digested. RNA-specific magnetic beads were used to recover and purify the rRNA-depleted total RNA. The purified total RNA was fragmented and in a reverse transcription reaction using random primers and actinomycin D. RNA was converted into single-stranded cDNA and subsequently converted into double-stranded cDNA in a second-strand cDNA synthesis reaction using dUTP to achieve strand specificity. The cDNA fragments were extended with a single adenosine base to the 3′ ends of the blunt-ended cDNA fragments after which pre-index anchors were ligated preparing the fragments for dual indexing. Anchor-ligated fragments were then purified using magnetic beads. Finally, enrichment PCR was carried out to enrich those DNA fragments that have anchor-ligated DNA fragments and to add indexes and primer sequences for cluster generation.

Sequencing. Purified dual-indexed sequence-libraries of each sample were equimolarly pooled and sequenced on Illumina MiSeq v2 300 Micro kit, paired end 150 reads (151-10-10-151)) at the VIB Nucleomics Core (https://nucleomicscore.sites.vib.be/en).

Data preprocessing. Low quality ends and adapter sequences were trimmed off from the Illumina reads with FastX 0.0.14[58] and Cutadapt 1.15[59]. Subsequently, small reads (length <35 bp), polyA-reads (more than 90 % of the bases equal A), ambiguous reads (containing N), low-quality reads (more than 50 % of the bases <Q25), and artifact reads (all but three bases in the read equal one base type) were filtered using FastX 0.0.14 and ShortRead 1.40.0[60]. With Bowtie2 2.3.3.1 we identified and removed reads that align to phix_illumina[61].

Read mapping. The preprocessed reads were aligned with bowtie2 2.3.3.1 to the reference genome of escherichia coli k12 (GCA000005845.ASM584v2) using the following options '--rf ---seed 1 -L 12 -k 20 --local'. Using Samtools 1.5, reads with a mapping quality smaller than 20 were removed from the alignments[62].

Read counting. The number of reads in the alignments that overlap with gene features were counted with featureCounts 1.5.3[63]. We removed genes for which all samples had less than 1 count-per-million. Raw counts were further corrected within samples for GC-content and between samples using full quantile normalization, as implemented in the EDASeq 2.32 package from Bioconductor[64].

Differential gene expression. With the EdgeR 3.26.8 package of Bioconductor, a negative binomial generalized linear model (GLM) was fitted against the normalized counts[65]. We did not use the normalized counts directly but worked with offsets. Differential expression was tested for with a GLM likelihood ratio test, also implemented in the EdgeR package. The resulting p-values were corrected for multiple testing with Benjamini-Hochberg to control the false discovery rate[66].

Reporting summary

Further information on research design is available in the Nature Portfolio Reporting Summary linked to this article.

Data availability

The proteomics data generated in this study have been deposited in the PRIDE database under accession code PXD056779 (https://doi.org/10.6019/PXD056779). The RNA-seq data generated in this study have been deposited in the GEO database under accession code GSE278706 (https://doi.org/10.6019/GSE278706). Additional data generated in this study are provided in the Supplementary Information and the Source Data file. Source data are provided in this paper.

References

1. Aloke, C. & Achilonu, I. Coping with the ESKAPE pathogens: Evolving strategies, challenges and future prospects. *Micro. Pathog.* **175**, 105963 (2023).
2. Venkateswaran, P. et al. Revisiting ESKAPE Pathogens: virulence, resistance, and combating strategies focusing on quorum sensing. *Front Cell Infect. Microbiol*. **13**, 1159798 (2023).
3. Darby, E. M. et al. Molecular mechanisms of antibiotic resistance revisited. *Nat. Rev. Microbiol*. **21**, 280–295 (2023).
4. Antimicrobial Resistance, C. Global burden of bacterial antimicrobial resistance in 2019: a systematic analysis. *Lancet* **399**, 629–655 (2022).
5. De Oliveira, D. M. P. et al. Antimicrobial Resistance in ESKAPE Pathogens. *Clin. Microbiol. Rev.* **33**, https://doi.org/10.1128/CMR.00181-19 (2020).
6. Leon-Buitimea, A., Garza-Cardenas, C. R., Garza-Cervantes, J. A., Lerma-Escalera, J. A. & Morones-Ramirez, J. R. The Demand for New Antibiotics: Antimicrobial Peptides, Nanoparticles, and Combinatorial Therapies as Future Strategies in Antibacterial Agent Design. *Front Microbiol* **11**, 1669 (2020).
7. Lata, M. et al. Evolutionary and in silico guided development of novel peptide analogues for antibacterial activity against ESKAPE pathogens. *Curr. Res Micro. Sci.* **4**, 100183 (2023).
8. Lazzaro, B. P., Zasloff, M. & Rolff, J. Antimicrobial peptides: Application informed by evolution. *Science* **368**, https://doi.org/10.1126/science.aau5480 (2020).
9. Huan, Y., Kong, Q., Mou, H. & Yi, H. Antimicrobial Peptides: Classification, Design, Application and Research Progress in Multiple Fields. *Front Microbiol* **11**, 582779 (2020).
10. Cardoso, M. H. et al. Non-Lytic Antibacterial Peptides That Translocate Through Bacterial Membranes to Act on Intracellular Targets. *Int. J. Mol. Sci*. **20**, https://doi.org/10.3390/ijms20194877 (2019).
11. Bucker, R. et al. The Cryo-EM structures of two amphibian antimicrobial cross-beta amyloid fibrils. *Nat. Commun.* **13**, 4356 (2022).
12. Khodaparast, L. et al. Exploiting the aggregation propensity of beta-lactamases to design inhibitors that induce enzyme misfolding. *Nat. Commun.* **14**, 5571 (2023).
13. Michiels, E. et al. Reverse engineering synthetic antiviral amyloids. *Nat. Commun.* **11**, 2832 (2020).
14. Khodaparast, L. et al. Aggregating sequences that occur in many proteins constitute weak spots of bacterial proteostasis. *Nat. Commun.* **9**, 866 (2018).
15. Gallardo, R. et al. De novo design of a biologically active amyloid. *Science* **354**, https://doi.org/10.1126/science.aah4949 (2016).
16. Janssen, K. et al. Exploiting the intrinsic misfolding propensity of the KRAS oncoprotein. *Proc. Natl Acad. Sci. USA* **120**, e2214921120 (2023).
17. Khodaparast, L. et al. Bacterial protein homeostasis disruption as a therapeutic intervention. *Front Mol. Biosci.* **8**, 681855 (2021).
18. Louros, N., Schymkowitz, J. & Rousseau, F. Mechanisms and pathology of protein misfolding and aggregation. *Nat. Rev. Mol. Cell Biol.* **24**, 912–933 (2023).
19. Wu, G. et al. Investigating the mechanism of action of aggregation-inducing antimicrobial Pept-ins. *Cell Chem. Biol.* **28**, 524–536.e524 (2021).
20. Aslund, A. et al. Studies of luminescent conjugated polythiophene derivatives: enhanced spectral discrimination of protein conformational states. *Bioconjug Chem.* **18**, 1860–1868 (2007).
21. Langenberg, T. et al. Thermodynamic and evolutionary coupling between the native and amyloid state of globular proteins. *Cell Rep.* **31**, 107512 (2020).
22. Duverger, W. et al. An end-to-end approach for single-cell infrared absorption spectroscopy of bacterial inclusion bodies: from AFM-IR

measurement to data interpretation of large sample sets. *J. Nanobiotechnol.* **22**, 406 (2024).
23. Piantavigna, S. et al. A mechanistic investigation of cell-penetrating Tat peptides with supported lipid membranes. *Biochim Biophys. Acta* **1808**, 1811–1817 (2011).
24. Knappe, D. et al. Oncocin (VDKPPYLPRPRPPRRIYNR-NH2): a novel antibacterial peptide optimized against gram-negative human pathogens. *J. Med Chem.* **53**, 5240–5247 (2010).
25. Czihal, P. et al. Api88 is a novel antibacterial designer peptide to treat systemic infections with multidrug-resistant Gram-negative pathogens. *ACS Chem. Biol.* **7**, 1281–1291 (2012).
26. Mechler, A. et al. Specific and selective peptide-membrane interactions revealed using quartz crystal microbalance. *Biophys. J.* **93**, 3907–3916 (2007).
27. McCubbin, G. A. et al. QCM-D fingerprinting of membrane-active peptides. *Eur. Biophys. J.* **40**, 437–446 (2011).
28. Shirani, H. et al. A Palette of Fluorescent Thiophene-Based Ligands for the Identification of Protein Aggregates. *Chemistry* **21**, 15133–15137 (2015).
29. Carattoli, A. Plasmids and the spread of resistance. *Int. J. Med. Microbiol.* **303**, 298–304 (2013).
30. Sun, D., Jeannot, K., Xiao, Y. & Knapp, C. W. Vol. 10, 1933 (Frontiers Media SA, 2019).
31. Sharma, S. et al. Microbial Biofilm: A Review on Formation, Infection, Antibiotic Resistance, Control Measures, and Innovative Treatment. *Microorganisms* **11**, https://doi.org/10.3390/microorganisms11061614 (2023).
32. Singh, A., Upadhyay, V., Upadhyay, A. K., Singh, S. M. & Panda, A. K. Protein recovery from inclusion bodies of Escherichia coli using mild solubilization process. *Micro. Cell Fact.* **14**, 41 (2015).
33. Kurt, N., Mounce, B. C., Ellison, P. A. & Cavagnero, S. Residue-specific contact order and contact breadth in single-domain proteins: Implications for folding as a function of chain elongation. *Biotechnol. Prog.* **24**, 570–575 (2008).
34. Ivankov, D. N. et al. Contact order revisited: influence of protein size on the folding rate. *Protein Sci.* **12**, 2057–2062 (2003).
35. Plaxco, K. W., Simons, K. T. & Baker, D. Contact order, transition state placement and the refolding rates of single domain proteins. *J. Mol. Biol.* **277**, 985–994 (1998).
36. Lin, J., Zhou, D., Steitz, T. A., Polikanov, Y. S. & Gagnon, M. G. Ribosome-targeting antibiotics: modes of action, mechanisms of resistance, and implications for drug design. *Annu. Rev. Biochem* **87**, 451–478 (2018).
37. Filbeck, S., Cerullo, F., Pfeffer, S. & Joazeiro, C. A. P. Ribosome-associated quality-control mechanisms from bacteria to humans. *Mol. Cell* **82**, 1451–1466 (2022).
38. Gottesman, S., Roche, E., Zhou, Y. & Sauer, R. T. The ClpXP and ClpAP proteases degrade proteins with carboxy-terminal peptide tails added by the SsrA-tagging system. *Genes Dev.* **12**, 1338–1347 (1998).
39. Ganesan, A. et al. Structural hot spots for the solubility of globular proteins. *Nat. Commun.* **7**, 10816 (2016).
40. Houben, B. et al. Autonomous aggregation suppression by acidic residues explains why chaperones favour basic residues. *EMBO J.*, e102864 (2020).
41. Arenz, S. & Wilson, D. N. Bacterial Protein Synthesis as a Target for Antibiotic Inhibition. *Cold Spring Harb. Perspect. Med.* **6**, https://doi.org/10.1101/cshperspect.a025361 (2016).
42. Pathak, B. K., Mondal, S., Banerjee, S., Ghosh, A. N. & Barat, C. Sequestration of Ribosome during Protein Aggregate Formation: Contribution of ribosomal RNA. *Sci. Rep.* **7**, 42017 (2017).
43. Tye, B. W. et al. Proteotoxicity from aberrant ribosome biogenesis compromises cell fitness. *Elife* **8**, https://doi.org/10.7554/eLife.43002 (2019).
44. UniProt, C. The universal protein resource (UniProt). *Nucleic Acids Res.* **36**, D190–D195 (2008).
45. Fernandez-Escamilla, A. M., Rousseau, F., Schymkowitz, J. & Serrano, L. Prediction of sequence-dependent and mutational effects on the aggregation of peptides and proteins. *Nat. Biotechnol.* **22**, 1302–1306 (2004).
46. Yu, G., Wang, L.-G., Han, Y. & He, Q.-Y. clusterProfiler: an R package for comparing biological themes among gene clusters. *Omics: J. Integr. Biol.* **16**, 284–287 (2012).
47. Osorio, D., Rondón-Villarreal, P. & Torres, R. Peptides: a package for data mining of antimicrobial peptides. *Small* **12**, 44–444 (2015).
48. Kabsch, W. & Sander, C. Dictionary of protein secondary structure: pattern recognition of hydrogen-bonded and geometrical features. *Biopolymers* **22**, 2577–2637 (1983).
49. Joosten, R. P. et al. A series of PDB related databases for everyday needs. *Nucleic Acids Res.* **39**, D411–D419 (2011).
50. Jumper, J. et al. Highly accurate protein structure prediction with AlphaFold. *Nature* **596**, 583–589 (2021).
51. Varadi, M. et al. AlphaFold Protein Structure Database: massively expanding the structural coverage of protein-sequence space with high-accuracy models. *Nucleic Acids Res.* **50**, D439–D444 (2022).
52. Baba, T. et al. Construction of Escherichia coli K-12 in-frame, single-gene knockout mutants: the Keio collection. *Mol. Syst. Biol.* **2**, 2006 0008 (2006).
53. Swings, T. et al. CRISPR-FRT targets shared sites in a knock-out collection for off-the-shelf genome editing. *Nat. Commun.* **9**, 2231 (2018).
54. Green, R. & Rogers, E. J. Transformation of chemically competent E. coli. *Methods Enzymol.* **529**, 329–336 (2013).
55. Reisch, C. R. & Prather, K. L. The no-SCAR (Scarless Cas9 Assisted Recombineering) system for genome editing in Escherichia coli. *Sci. Rep.* **5**, 15096 (2015).
56. Ritchie, M. E. et al. limma powers differential expression analyses for RNA-sequencing and microarray studies. *Nucleic acids Res.* **43**, e47–e47 (2015).
57. Sonderby, T. V. et al. Sequence-targeted Peptides Divert Functional Bacterial Amyloid Towards Destabilized Aggregates and Reduce Biofilm Formation. *J. Mol. Biol.*, 168039 (2023).
58. Pearson, W. R., Wood, T., Zhang, Z. & Miller, W. Comparison of DNA sequences with protein sequences. *Genomics* **46**, 24–36 (1997).
59. Martin, M. Cutadapt removes adapter sequences from high-throughput sequencing reads. *2011* **17**, 3 (2011).
60. Morgan, M. et al. ShortRead: a bioconductor package for input, quality assessment and exploration of high-throughput sequence data. *Bioinformatics* **25**, 2607–2608 (2009).
61. Langmead, B. & Salzberg, S. L. Fast gapped-read alignment with Bowtie 2. *Nat. Methods* **9**, 357–359 (2012).
62. Li, H. et al. The Sequence Alignment/Map format and SAMtools. *Bioinformatics* **25**, 2078–2079 (2009).
63. Liao, Y., Smyth, G. K. & Shi, W. featureCounts: an efficient general purpose program for assigning sequence reads to genomic features. *Bioinformatics* **30**, 923–930 (2014).
64. Risso, D., Schwartz, K., Sherlock, G. & Dudoit, S. GC-content normalization for RNA-Seq data. *BMC Bioinforma.* **12**, 480 (2011).
65. Robinson, M. D., McCarthy, D. J. & Smyth, G. K. edgeR: a Bioconductor package for differential expression analysis of digital gene expression data. *Bioinformatics* **26**, 139–140 (2010).
66. Benjamini, Y. & Hochberg, Y. Controlling the false discovery rate - a practical and powerful approach to multiple testing. *J. R. Stat. Soc. Ser. B-Stat. Methodol.* **57**, 289–300 (1995).

Acknowledgements

The Switch Laboratory was supported by the Flanders Institute for Biotechnology (VIB, C0401), KU Leuven through postdoctoral grant PDMT2/24/084 to R.D., and the Fund for Scientific Research Flanders (FWO), through project grants I011220N to F.R. and G045920N, G053420N and G0A6724N to J.S.; through PhD fellowship 1128822N to W.D. and through

postdoctoral fellowships 1231021N to Lad. K., 12S3722N to B.H., and 1223924N to K.K. We thank the following core facilities for training, technical support, and access to their instrument parks: the VIB BioImaging Core at KU Leuven, the KU Leuven Flow, and Mass Cytometry Facility, the VIB Nucleomics Core and the Electron Microscopy Core of VIB- KU Leuven. We thank Kathleen Sonck and Veerle Rober for assistance with bacterial load determination in the in vivo experiments and Dr. Stefanie Desmet (University Hospitals, Leuven) for kindly providing clinical isolates. Library preparation, sequencing, and statistical data analysis were performed by VIB Nucleomics Core (https://nucleomicscore.sites.vib.be/en).

Author contributions

F.R. and J.S. designed and fund-raised the study. Lal. K., Lad. K., F.N., B.H., T.S., J.M., S.C., L.M., B.S., F.R., and J.S. designed the experiments and Lal. K., Lad. K. and G.W. performed all microbiological experiments and designed and conducted the animal experiments. M.D.V. performed peptide synthesis, purification, and quality control, W.D. performed AFM-IR experiment and data analysis, M.C. performed Quartz Microbalance experiments, R.D., K.K., D.C., L.M., J.S., and F.R. performed data analysis. Lal. K., Lad. K., R.D., J.S., and F.R. wrote the manuscript and all authors provided input and proofread the manuscript.

Competing interests

Lal. K., Lad. K., F.R., and J.S. are inventors on a patent filed by the host institution VIB describing the sequence of P33. The remaining authors declare no competing interests.

Additional information

Supplementary information The online version contains supplementary material available at https://doi.org/10.1038/s41467-025-56873-z.

Correspondence and requests for materials should be addressed to Joost Schymkowitz or Frederic Rousseau.

Peer review information *Nature Communications* thanks Reynald Gillet, and the other, anonymous, reviewers for their contribution to the peer review of this work. A peer review file is available.